International Journal of Heat and Technology
Vol. 44, No. 2, April, 2026, pp. 733-758
Journal homepage: http://iieta.org/journals/ijht

Magnetohydrodynamic Hybrid Nanofluid Convection and Entropy Generation in Annular Porous Channels with Radiation

Ali Muslem Abed, Eman Shaker Hussein, Shaymaa Hamza Anbr Swadi, Ahmed M. Hassan*, Naseer H. Hamza

Department of Mechanical Engineering, University of Al-Qadisiyah, Ad-Diwaniyah 58001, Iraq

Corresponding Author Email: ahmed.mohammed.hassan@qu.edu.iq

https://doi.org/10.18280/ijht.440225

Received: 4 February 2026
Revised: 12 April 2026
Accepted: 22 April 2026
Available online: 30 April 2026

Keywords:
porous media, hybrid nanofluid, radiation, entropy generation, Magnetohydrodynamic, free convection

ABSTRACT

This study numerically investigates magnetohydrodynamic (MHD) natural convection of an Ag–MgO/water hybrid nanofluid in a double-pipe heat exchanger incorporating four distinct porous layer configurations under the combined effects of radiation and electromagnetic forces. The governing equations, including the Darcy porous-media model and the Rosseland radiation approximation, are solved using the Galerkin weighted-residual finite element method (FEM). The analysis examines how the geometric arrangement of the porous layers interacts with buoyancy, magnetic, nanoparticle, and radiative effects over wide ranges of the controlling dimensionless parameters. The results reveal that the porous-layer distribution is the dominant factor governing thermal performance: the diagonal arrangement enhances heat transfer by up to 29.5%, whereas the bottom-half configuration reduces it by 20.3%. Moderate magnetic fields (Ha ≈ 30) suppress entropy generation by as much as 73%, while stronger fields reverse this trend. Hybrid nanoparticle loading in symmetrical configurations improves heat transfer by 10.6% and concurrently lowers entropy generation by 5.6%. The orientation of the magnetic field exerts a negligible thermal influence (< 0.5%), whereas radiation effects are strongly configuration-dependent. These findings offer practical design guidelines for optimizing annular heat exchangers in energy-conversion and thermal-management systems where a balanced trade-off between heat transfer enhancement and thermodynamic efficiency is essential.

1. INTRODUCTION

Thermal enhancement has been extensively investigated by researchers aiming to improve the performance of applications that rely on heat transfer phenomena. Some of these examples include heat exchangers [1-3], solar collectors [4-7], boilers of power plants [8-10], cooling systems, and nuclear reactors [11-14].

Porous media are any materials that allow fluids to penetrate through their pores. There are many types of porous media depending on the materials that are used to manufacture them and the properties of the porous media, such as porosity and permeability [15-17]. Adding porous media can control heat enhancement depending on the material and its properties [18-20]. Heat enhancement in an enclosure filled with saturated porous material was explored by Groşan et al. [21]. Increasing the Rayleigh number was found to enhance heat transfer; moreover, the influence of the porous material becomes significant only when the porous structure exhibits high thermal conductivity. Baytaş and Pop [22] studied natural convection in an enclosure filled with porous media. The results stated an enhancement in heat transfer with an increase in Ra number, while an inverse relationship with increasing Darcy number. Another investigation by Beckermann et al. [23] explored free convection in a porous enclosure. The results yielded similar findings to those of previous research regarding Ra and Da numbers. However, these foundational studies have largely focused on uniformly filled porous enclosures, leaving the influence of spatially distributed or partial porous layers within annular geometries largely unexplored.

The thermal performance of conventional working fluids, such as water or oil, can be enhanced by the addition of nanoparticles with superior thermophysical properties [24-27]. Authors have explored many types of nanoparticles, including Cu, Ag, Al_2O_3, TiO_2, etc. [28-34]. Free convection in a cavity filled with Cu/water nanofluid was numerically explored by Rashad et al. [35]. The authors revealed that heat transfer improved by adding the nanoparticles, and this enhancement increased with the increase in volume concentration. Another investigation was conducted by Nayak et al. [36], who examined the addition of Al_2O_3 to the working fluid, water, and found that it highly improved the transformation of heat. Furthermore, researchers have explored adding more than one type of nanoparticle to the working fluid, which is referred to as a hybrid nanofluid [37]. Turabi et al. [38] examined the addition of a hybrid nanofluid, consisting of Al_2O_3 and Cu, to the working fluid in a staggered cavity. The results clearly

show that increasing the nanoparticle concentration enhances the transformation of heat while also increasing the entropy generation. Khatun et al. [39] numerically investigated the effect of adding SiO_2 and Ag to the working fluid, water, at different concentrations (0-0.1). The results indicated that the enhancement of heat transfer increased by 11.29% when the hybrid nanofluid was added. Another hybrid nanofluid, Cu-TiO_2-H_2O, was investigated by Aissa et al. [40] in an octagonal enclosure. The results stated that heat transfer was significantly increased by adding nanoparticles. Despite these advances, the combined interaction between hybrid nanoparticle loading and non-uniform porous-layer arrangements in annular geometries has not been systematically addressed.

Magnetohydrodynamic (MHD) effects play a significant role in controlling thermal and fluid flow behavior, which encourages researchers to explore this area extensively [41-46]. Natural convection under the influence of the MHD was studied by Kefayati [47], who explored the application of different MHD strengths. Heat transfer was markedly reduced in the presence of MHD, and the drop increased with the rise of the Ha number. These results were confirmed by Devi et al. [48], who numerically investigated free convection in a square-shaped enclosure and reported that heat transfer declines progressively as the Hartmann number increases. Nevertheless, most of these investigations have been limited to simple rectangular or square enclosures with uniform or no porous media, and the coupled effects of magnetic-field orientation, radiation, and hybrid nanoparticle loading in partially porous annular geometries remain insufficiently quantified, particularly from a second-law (entropy generation) perspective.

Despite the extensive body of literature reviewed above, a critical examination reveals four specific gaps that motivate the present study. First, the majority of prior investigations have considered either fully porous or fully open cavities, whereas the practically important case of spatially distributed porous layers within an annular double-pipe geometry has received limited attention. Second, the interaction between hybrid nanoparticle loading (specifically Ag–MgO/water) and non-uniform porous-layer arrangements under combined MHD and radiative effects has not been systematically characterised. Third, existing entropy-generation analyses rarely treat the porous-layer distribution as a design variable, and the non-monotonic response of total irreversibilities to increasing magnetic-field strength remains poorly understood. Fourth, the role of magnetic-field orientation, as distinct from its magnitude, has been largely neglected in hybrid-nanofluid porous annular configurations. The present study addresses these four gaps simultaneously through a comprehensive finite-element investigation that systematically quantifies the influence of porous-layer distribution, Rayleigh and Darcy numbers, Hartmann number and field orientation, nanoparticle volume fraction, and radiation parameters on the heat-transfer performance and entropy generation of an Ag–MgO/water hybrid nanofluid in an annular heat exchanger.

2. PROBLEM FORMULATION

2.1 Physical description of the case study

The physical configuration consists of an annular cavity comprising an inner hot cylinder concentrically positioned within an outer cold cylinder. The outer shell consists of multiple sections of porous media along it, which provide sufficient permeability for fluid flow through it—a configuration relevant to numerous engineering applications, including filtration systems, heat exchangers, and fuel cells. Since the geometry and flow conditions are symmetric and uniform along the third dimension (depth), the problem can be represented in two-dimensional geometry, as shown in Figure 1, without significantly compromising the accuracy of estimating the thermophysical characteristics of the flow. Thus, the outer cold circular cavity with a diameter D is eccentric with a hot circular domain of diameter 0.2D. The flowing fluid, which is a nanofluid, consists of a carrier water-based fluid and added hybrid nanoparticles of MgO and Ag. The working fluid is in thermal equilibrium with its components and with the porous media. Due to the high dilution, the nanofluid is taken as incompressible, single-phase, and Newtonian. The nanoparticles are of the same size and shape, and the porous medium is isotropic and homogeneous. All thermophysical features, except density, are assumed constant. The change in density is modeled by the Boussinesq approximation. An inclined external field of magnetism is applied to the whole geometry and acts upon the working fluid and porous media.

The investigation considers four distinct configurations: the first comprises four equal 45° porous sectors uniformly distributed around the annulus, with the remaining sectors serving as free-flow passages. In the second case, two equal quadrants of porous media with a 90-degree sector are distributed laterally. The third and fourth cases are the semi-circular sector of porous media and the semi-circular sector of free passage in the top and lateral orientations, as clearly illustrated in Figure 1.

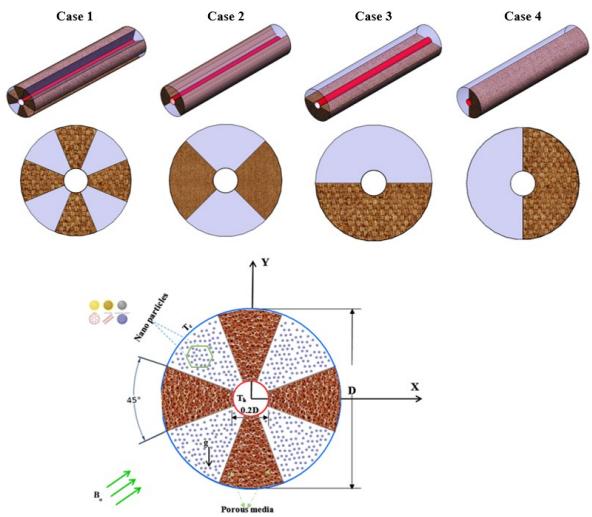

Figure 1. Schematic configuration of the physical model

2.2 Governing equations

To analyse the thermal behaviour of the hybrid nanofluid within the computational domain, the Navier–Stokes governing equations for mass, momentum, and energy conservation are employed. The case study consists of two zones: one with free passages and the other containing porous media. The following vector equations are applied in the non-porous regions:

$$\nabla(\tilde{\rho}V) = 0 \tag{1}$$

$$\tilde{\rho}(\mathrm{V}.\nabla V) = -\nabla P + \tilde{\mu}\nabla^2 V + F \tag{2}$$

where, F is the external magnetic and buoyancy effect.

$$\mathrm{V}.\nabla T = \tilde{\alpha}\nabla^2 T + \nabla q_r \tag{3}$$

The abovementioned vector form of governing equations can be extracted in Cartesian coordinates as follows [49]:

$$\tilde{\rho}\left(\frac{\partial \tilde{u}}{\partial x} + \frac{\partial \tilde{v}}{\partial y}\right) = 0 \tag{4}$$

$$\begin{aligned}\tilde{u}\frac{\partial \tilde{u}}{\partial x} + \tilde{v}\frac{\partial \tilde{u}}{\partial y} = &-\frac{1}{\rho_{nf}}\frac{\partial p}{\partial x} + \nu\left(\frac{\partial^2 \tilde{u}}{\partial x^2} + \frac{\partial^2 \tilde{u}}{\partial y^2}\right) + \\ &\frac{\tilde{\sigma}{B_o}^2}{\tilde{\rho}} sin(\gamma)(\tilde{v}\, cos(\gamma) - \tilde{u}\, sin(\gamma))\end{aligned} \tag{5}$$

$$\begin{aligned}\tilde{u}\frac{\partial \tilde{v}}{\partial x} + \tilde{v}\frac{\partial \tilde{v}}{\partial y} = &-\frac{1}{\rho_{nf}}\frac{\partial p}{\partial y} + \nu\left(\frac{\partial^2 \tilde{v}}{\partial x^2} + \frac{\partial^2 \tilde{v}}{\partial y^2}\right) \\ &+ g\frac{\widetilde{(\rho\beta_T)}}{\tilde{\rho}}(T - T_c) \\ &+ \frac{\tilde{\sigma}{B_o}^2}{\rho_{nf}} cos(\gamma)(\tilde{u}\, sin(\gamma) \\ &- \tilde{v}\, cos(\gamma))\end{aligned} \tag{6}$$

The energy equation accounts for the conservation of energy, can be written as:

$$\tilde{u}\frac{\partial \tilde{T}}{\partial x} + \tilde{v}\frac{\partial \tilde{T}}{\partial y} = \tilde{\alpha}\left(\frac{\partial^2 \tilde{T}}{\partial x^2} + \frac{\partial^2 \tilde{T}}{\partial y^2}\right) - \left(\frac{\partial q_{rx}}{\partial x} + \frac{\partial q_{ry}}{\partial y}\right) \tag{7}$$

For porous regions, the governing equations can be formulated as follows [50-52]:

$$\frac{\partial \hat{u}}{\partial x} + \frac{\partial \hat{v}}{\partial y} = 0 \tag{8}$$

$$\begin{aligned}\hat{u}\frac{\partial \hat{u}}{\partial x} + \hat{v}\frac{\partial \hat{u}}{\partial y} = &-\frac{1}{\rho_{nf}}\frac{\partial p}{\partial x} + \hat{v}\left(\frac{\partial^2 \hat{u}}{\partial x^2} + \frac{\partial^2 \hat{u}}{\partial y^2}\right) - \frac{\tilde{\mu}}{\rho_{nf}}\frac{\hat{u}}{K} \\ &+ \frac{\hat{\sigma}{B_o}^2}{\rho_{nf}} sin(\gamma)(\hat{v}\, cos(\gamma) \\ &- \hat{u}\, sin(\gamma))\end{aligned} \tag{9}$$

$$\begin{aligned}\hat{u}\frac{\partial \hat{v}}{\partial x} + \hat{v}\frac{\partial \hat{v}}{\partial y} = &-\frac{1}{\rho_{nf}}\frac{\partial p}{\partial y} + \hat{v}\left(\frac{\partial^2 \hat{v}}{\partial x^2} + \frac{\partial^2 \hat{v}}{\partial y^2}\right) \\ &+ g\frac{(\rho\beta_T)_{nf}}{\rho_{nf}}(T - T_c) - \frac{\mu_{nf}}{\tilde{\rho}}\frac{\hat{v}}{K} \\ &+ \frac{\hat{\sigma}{B_o}^2}{\rho_{nf}} cos(\gamma)(\hat{u}\, sin(\gamma) \\ &- \hat{v}\, cos(\gamma))\end{aligned} \tag{10}$$

The energy equation accounts for the conservation of energy and is given by [53]:

$$\begin{aligned}\hat{u}\frac{\partial \hat{T}}{\partial x} + \hat{v}\frac{\partial \hat{T}}{\partial y} = &\frac{k_{eff}}{\widetilde{\rho_{nf}cp}}\left(\frac{\partial^2 \hat{T}}{\partial x^2} + \frac{\partial^2 \hat{T}}{\partial y^2}\right) \\ &-\left(\frac{\partial q_{rx}}{\partial x} + \frac{\partial q_{ry}}{\partial y}\right)\end{aligned} \tag{11}$$

In this study, it is accounted for the radiation effect, and it can be expressed as indicated by Uddin et al. [54]:

$$q_{rx} = \frac{16{T_c}^3}{3\beta}\frac{\partial T}{\partial x}, q_{ry} = \frac{16{T_c}^3}{3\beta}\frac{\partial T}{\partial y} \tag{12}$$

where, Superscript $\tilde{}$ refer to the hybrid nanofluid, Superscript $\hat{}$ refer to porous media.

Treatment of the free–porous interface. The coupling between the free-flow region (Eqs. (4)-(7)) and the porous region (Eqs. (8)-(12)) is accomplished through the Brinkman-extended Darcy formulation adopted for the porous medium. Because the Brinkman term retains the viscous Laplacian in the momentum equation, the porous-region equations remain of the same differential order as the Navier–Stokes equations in the free region, and the solution fields are continuous across the interface without requiring ad-hoc matching relations. Consequently, the following physical continuity conditions are automatically enforced at the free–porous boundary:

(i) continuity of the velocity components, $u_f = u_p$ and $v_f = v_p$.

(ii) continuity of the total stress, including the Brinkman viscous contribution, $\mu_{hnf}(\partial u/\partial n)_f = \mu_{eff}(\partial u/\partial n)_p$.

where n denotes the direction normal to the interface;

(iii) continuity of temperature under the local thermal-equilibrium assumption, $T_f = T_p$.

(iv) continuity of the conductive heat flux, $k_{hnf}(\partial T/\partial n)_f = k_{eff}(\partial T/\partial n)_p$, where k_{eff} is the effective thermal conductivity of the saturated porous region.

The subscripts "*f*" and "*p*" refer to the free-flow and porous sides of the interface, respectively. This treatment is consistent with the one-domain approach widely adopted for coupled free–porous convection problems.

For more reliable and efficient process of simulation to determine thermophysical behavior by using the following intermediate variables:

$$X = \frac{x}{W},\ Y = \frac{y}{W},\ U = \frac{uW}{\alpha_f},\ V = \frac{vW}{\alpha_f},\ \theta = \frac{T - T_c}{T_h - T_c},\ P = \frac{pW^2}{\rho_{nf}\alpha_f^2},$$
$$Ra = \frac{g\,\beta_T(T_h - T_c)W^3}{\nu_f^2}\,Pr,\ Pr = \frac{\nu_f}{\alpha_f},\ Da = \frac{K}{W^2},\ \lambda = \frac{QW^2}{k},\ Rd = \frac{4\sigma_B {T_c}^3}{k\beta}, Ha = B_o W\sqrt{\frac{\sigma_{nf}}{\rho_{nf}\nu_{nf}}}$$

and thus, the governing equations in their non-dimensional form:

-For hybrid Nano-fluid

$$\frac{\partial \tilde{U}}{\partial X} + \frac{\partial \tilde{V}}{\partial Y} = 0 \tag{13}$$

$$\begin{aligned}\tilde{U}\frac{\partial \tilde{U}}{\partial X} + \tilde{V}\frac{\partial \tilde{U}}{\partial Y} = &-\frac{\partial P}{\partial X} + \frac{\nu_{nf}}{\nu_f}Pr\left(\frac{\partial^2 \tilde{U}}{\partial X^2} + \frac{\partial^2 \tilde{U}}{\partial Y^2}\right) \\ &+ \frac{\rho_f}{\rho_{nf}}Pr\,Ha^2\, sin(\gamma)(\tilde{V}\, cos(\gamma) \\ &- \tilde{U}\, sin(\gamma))\end{aligned} \tag{14}$$

$$\begin{aligned}\tilde{U}\frac{\partial \tilde{V}}{\partial X} + \tilde{V}\frac{\partial \tilde{V}}{\partial Y} = &-\frac{\partial P}{\partial Y} + \frac{\nu_{nf}}{\nu_f}Pr\left(\frac{\partial^2 \tilde{V}}{\partial X^2} + \frac{\partial^2 \tilde{V}}{\partial Y^2}\right) \\ &+ \frac{(\rho\beta_T)_{nf}}{\rho_{nf}\beta_f}\,Ra\,Pr\theta \\ &+ \frac{\rho_f}{\rho_{nf}}Pr\,Ha^2\, cos(\gamma)(\tilde{U}\, sin(\gamma) \\ &- \tilde{V}\, sin(\gamma))\end{aligned} \tag{15}$$

$$\tilde{U}\frac{\partial\theta}{\partial X}+\tilde{V}\frac{\partial\theta}{\partial Y}=\left(\frac{\tilde{\alpha}}{\alpha_f}+\frac{4\alpha_{nf}Rd}{3\alpha_f}\right)\left(\frac{\partial^2\theta}{\partial X^2}+\frac{\partial^2\theta}{\partial Y^2}\right)+\frac{\tilde{\alpha}}{\alpha_f}\lambda\theta \quad (16)$$

In Eq. (16), $\lambda = QW^2/k_f$ denotes the dimensionless heat-source parameter, where Q (W/m³·K) is the volumetric internal heat-generation coefficient. Positive values of λ correspond to internal heat generation (source), while negative values would represent a heat sink. In the present study, λ is varied within the range $1 \leq \lambda \leq 5$ to assess the effect of internal heat generation on the thermal and entropy-generation fields.

-For porous layer

$$\frac{\partial\hat{U}}{\partial X}+\frac{\partial\hat{V}}{\partial Y}=0 \quad (17)$$

$$\begin{aligned}\hat{U}\frac{\partial\hat{U}}{\partial X}+\hat{V}\frac{\partial\hat{U}}{\partial Y}=&-\frac{\partial P}{\partial X}+\frac{\tilde{\mu}}{\rho_{nf}\nu_f}Pr\left(\frac{\partial^2\hat{U}}{\partial X^2}+\frac{\partial^2\hat{U}}{\partial Y^2}\right)\\&-\frac{Pr}{Da}\hat{U}\\&+\frac{\tilde{\mu}}{\tilde{\rho}\nu_f}Pr\,Ha^2\,sin(\gamma)(\hat{V}\,cos(\gamma)\\&-\hat{U}\,sin(\gamma))\end{aligned} \quad (18)$$

$$\begin{aligned}\hat{U}\frac{\partial\hat{V}}{\partial X}+\hat{V}\frac{\partial\hat{V}}{\partial Y}=&-\frac{\partial P}{\partial Y}+\frac{\tilde{\mu}}{\rho_{nf}\nu_f}Pr\left(\frac{\partial^2\hat{V}}{\partial X^2}+\frac{\partial^2\hat{V}}{\partial Y^2}\right)\\&+\frac{(\rho\beta_T)_{nf}}{\rho_{nf}\beta_f}\,Ra\,Pr\,\theta-\frac{Pr}{Da}\hat{V}\\&+\frac{\tilde{\mu}}{\tilde{\rho}\nu_f}Pr\,Ha^2\,cos(\gamma)(\hat{U}\,sin(\gamma)\\&-\hat{V}\,sin(\gamma))\end{aligned} \quad (19)$$

$$\begin{aligned}\hat{U}\frac{\partial\theta}{\partial X}+\hat{V}\frac{\partial\theta}{\partial Y}=&\left(\frac{\alpha_{nf}}{\alpha_f}+\frac{4\tilde{V}k_{eff}Rd}{3\tilde{k}\alpha_f}\right)\left(\frac{\partial^2\theta}{\partial X^2}+\frac{\partial^2\theta}{\partial Y^2}\right)\\&+\frac{\tilde{V}}{\alpha_f}\frac{k_{eff}}{\tilde{k}}\lambda\theta\end{aligned} \quad (20)$$

The abovementioned governing equations are subjected to the following boundary conditions:

- at $\sqrt{X^2+Y^2}=0.2D \Rightarrow \theta=1,\ U=0,$ and $V=0.$
- at $\sqrt{X^2+Y^2}=D \Rightarrow \theta=0,\ U=0,$ and $V=0.$

to assess the heat transfer mechanisms between conduction and convection, the local and average Nusselt numbers are defined as follows:

$$Nu_L=-\left(\frac{\tilde{k}}{k_f}+\frac{4\tilde{k}}{3k_f}Rd\right)\frac{\partial\theta}{\partial s} \quad (21)$$

$$Nu_{avg}=\int_0^s Nu_L dS \quad (22)$$

where, s is the circular path of the inner cylinder

The stream function of flow is defined by:

$$\frac{\partial^2\psi}{\partial X^2}+\frac{\partial^2\psi}{\partial Y^2}=\frac{\partial U}{\partial Y}-\frac{\partial V}{\partial X} \quad (23)$$

The accompanying irreversibilities through the fluid circulation inside the geometry can be summarized in the thermal and frictional irreversibilities and are formulated as follows in non-dimensional form:

$$\begin{aligned}S'''_{\text{gen}}=&\frac{\tilde{k}}{k_f}\left[\left(\frac{\partial\theta}{\partial X}\right)^2+\left(\frac{\partial\theta}{\partial Y}\right)^2\right]\\&+\Xi\left[2\left(\frac{\partial U}{\partial X}\right)^2+2\left(\frac{\partial V}{\partial Y}\right)^2\right.\\&\left.+\left(\frac{\partial U}{\partial Y}+\frac{\partial V}{\partial X}\right)^2\right]\end{aligned} \quad (24)$$

where, Ξ is irreversibility factor and given by [53, 55, 56]:

$$\Xi=\frac{\tilde{\mu}T_0}{k_f}\left(\frac{U_0}{T_H-T_c}\right) \quad (25)$$

The non-dimensional total entropy generation $(\dot{S}_{\text{gen}})$ is given by:

$$\dot{S}_{gen}=\int S'''_{gen}dA \quad (26)$$

The dimensionless Bejan number, *Be*, determines the ratio between the thermal component and the total generated irreversibilities, and it can be articulated as [55, 57]:

$$Be=\frac{S'''_{gen,h}}{S'''_{\text{gen}}} \quad (27)$$

2.3 Physical properties of the hybrid nanofluid

The working fluid inside the geometry is water serving as the base carrier fluid, and magnesium oxide and silver nanoparticles that are suspended in it. These components can ensure a balance between thermal conductivity and specific heat capacity, thereby enhancing the thermophysical properties of the working fluid. Table 1 provides a detailed description of these properties.

Table 1. Properties of the components of hybrid nanofluid [58-60]

Properties	Water	Magnesium Oxide	Silver
$c_p(J.kg^{-1}.K^{-1})$	4179	879	235
$k\ (W.m^{-1}.K^{-1})$	0.613	30	429
$\alpha\ (m^2.s^{-1})$	1.47×10^{-7}	95.3×10^{-7}	174×10^{-3}
$\beta\ (K^{-1})$	21×10^{-5}	33.6×10^{-6}	$5.4^*\times10^{-5}$
$\rho\ (kg.m^{-3})$	997.1	3580	10500
$\mu\ (kg.m^{-1}.s^{-1})$	8.9×10^{-4}	--	--

To calculate the density of the hybrid nanofluid, superposition hypotheses can be used as follows:

$$\rho_{nf}=(1-\varphi)\rho_f+\varphi_{MgO}\rho_{\text{MgO}}+\varphi_{\text{Ag}}\rho_{\text{Ag}} \quad (28)$$

and the product of density and coefficient of thermal expansion is expressed as:

$$\begin{aligned}\widetilde{(\rho\beta)}=&(1-\varphi)(\rho\beta)_f+\varphi_{MgO}(\rho\beta)_{\text{MgO}}\\&+\varphi_{\text{Ag}}(\rho\beta)_{\text{Ag}}\end{aligned} \quad (29)$$

while the product of density and specific heat is expressed as:

$$\begin{aligned}\widetilde{(\rho c_p)}=&(1-\varphi)(\rho c_p)_f+\varphi_{\text{MgO}}(\rho c_p)_{\text{MgO}}\\&+\varphi_{\text{Ag}}(\rho c_p)_{\text{Ag}}\end{aligned} \quad (30)$$

and the thermal diffusivity:

$$\tilde{\alpha} = \frac{\tilde{k}}{(\widetilde{\rho c_p})} \tag{31}$$

On the other hand, Esfe et al. [58] calculated the viscosity and thermal conductivity experimentally and introduced the following relationships:

$$\frac{\tilde{\mu}}{\mu_f} = (1 + 32.795\tilde{\varphi} - 7214\tilde{\varphi}^2 + 714600\tilde{\varphi}^3 - 0.1941 \times 10^8\tilde{\varphi}^4)\ 0 \le \tilde{\varphi} \le 0.02 \tag{32}$$

$$\frac{\tilde{k}}{k_f} = \frac{0.1747 \times 10^5 + \tilde{\varphi}}{0.1747 \times 10^5 - 0.1498 \times 10^6\tilde{\varphi} + 0.1117 \times 10^7\tilde{\varphi}^2 + 0.1997 \times 10^8\tilde{\varphi}^3} \tag{33}$$

The choice of the Ag–MgO/water hybrid nanofluid as the working fluid in this study is motivated by its superior thermal behaviour relative to single-component nanofluids. Experimental investigations by Salho et al. [53], whose correlations are adopted in Eqs. (32)-(33), as well as numerical studies by Alomari et al. [59] and Ghalambaz et al. [60], have shown that the Ag–MgO combination benefits from a favourable synergy between the two constituents: silver provides a high thermal conductivity (k_{Ag} = 429 W/m·K) that enhances the effective conductivity of the suspension, while magnesium oxide contributes a higher specific heat capacity (c_p, MgO = 879 J/kg·K) that preserves the thermal inertia of the fluid. As a result, the hybrid formulation achieves a higher effective heat-transport performance than either Ag/water or MgO/water alone at the same total volume fraction, without an excessive viscosity penalty. This combined advantage makes the Ag–MgO/water hybrid particularly well suited to the annular heat-exchanger configurations examined in this work.

2.4 Numerical methodology and solution procedure

The numerical solution of the governing partial differential equations involves discretising the computational domain into small subdomains, known as finite elements. The finite element method (FEM) is a useful numerical technique that is used to solve coupled equations of momentum and energy in complex geometries. The process of finding a solution starts by turning the nonlinear partial differential equation into a set of linear algebraic equations that can be solved numerically. The continuity equation is used as a constraint, with a penalty parameter introduced to ensure its satisfaction. For all numerical calculations, the successive steps of solutions are said to be convergent when: $\left|\frac{\lambda_{i+1}-\lambda_i}{\lambda_{i+1}}\right| \le 10^{-6}$, where (λ) is any parameter.

2.5 Mesh independence test

The current domain of interest has been divided into small subdomains to ensure the accurate capture of physical phenomena. While smaller subdomains improve solution accuracy, they impose higher computational cost and runtime. Therefore, it is crucial to know when to stop dividing the domain into smaller ones. The average Nusselt number and total entropy were used in the mesh independence test. The size of the mesh is such that there is no significant change in the values of these parameters beyond it. The test is done at the following parameters: Ra = 10^4, Da = 0.001, Ha = 5, γ = 0, φ = 0.01, Rd = 1, λ = 1, with a size of 29036 elements. Table 2 and Figure 2 illustrate the test and the obtained numerical values. The grid distribution is depicted in Figure 3.

Table 2. Mesh independence test in terms of the average Nusselt number and the total entropy generation

Mesh Size	Number of Elements	Nu_{av}	Absolute Deviation (%)	S_{total}	Absolute Deviation (%)
M-1	220	13.088		141.71	
M-2	364	13.902	5.855273	150.34	5.740322
M-3	720	15.595	10.85604	160.01	6.043372
M-4	1300	16.629	6.218053	163.64	2.218284
M-5	1920	17.323	4.006234	165.64	1.207438
M-6	7688	18.970	8.68213	168.46	1.673988
M-7	29036	19.837	4.370621	169.10	0.378474

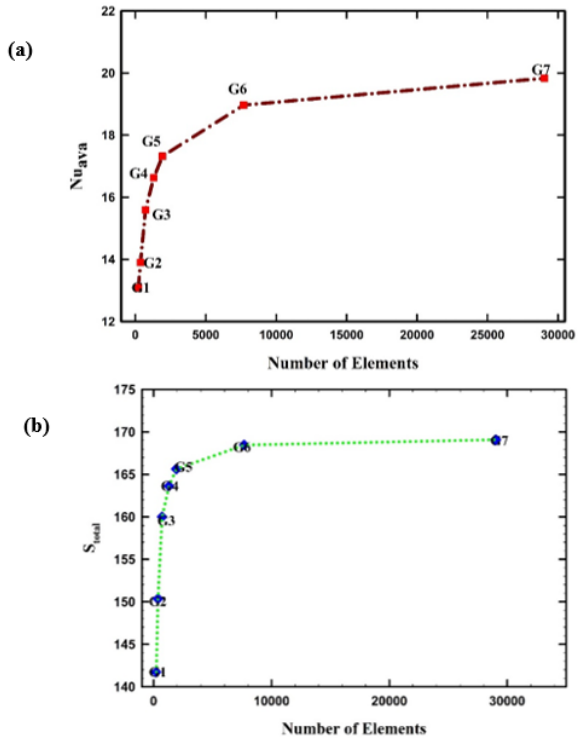

Figure 2. Grid independence: (a) For average nusulet number; (b) For entropy generation

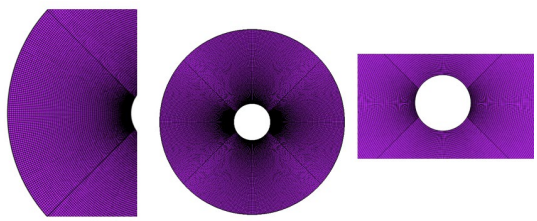

Figure 3. Grid distribution of the computational domain

2.6 Validation with previous work

To establish the reliability of our numerical approach, we conducted comprehensive validation against established experimental and numerical studies in the literature.

Figure 4 presents a comparative analysis of our computational results with those of Chen and Cheng [61], examining streamline distributions in a semicircular cavity. The close correspondence between our FEM code predictions and both the experimental observations and numerical solutions from Chen and Cheng [61] demonstrates the accuracy of our simulation methodology.

Further validation was performed by comparing the results with isothermal patterns. Figure 5 illustrates the consistency between our current isothermal distributions and those reported in both the numerical study by Alhashash and Saleh [62] and the experimental investigation by Kuehn and Goldstein [63], under identical parametric conditions (Ra = 9.52×10^4, Pr = 6.2). The similar isothermal patterns across all three studies confirm the thermal prediction capability of our numerical approach.

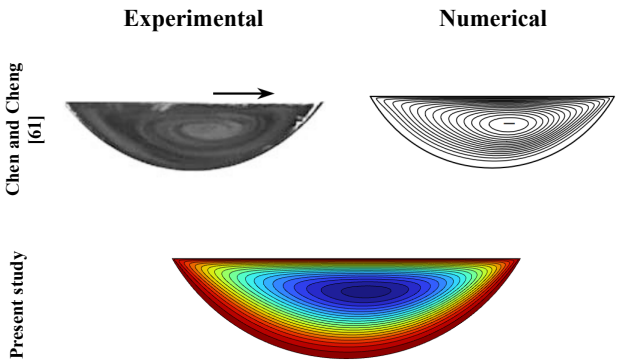

Figure 4. Validation of the present study code streamlines results with experimental and numerical results of Chen and Cheng [61]

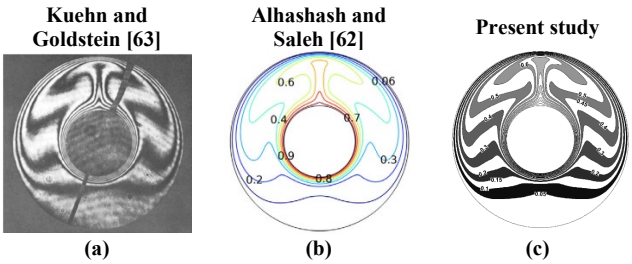

Figure 5. Verification isotherms of the current result (c), (a) with Kuehn and Goldstein [63], (b) Alhashash and Saleh [62]

Additional verification was conducted against the work of Basak et al. [64], focusing on flow and thermal fields in porous media-filled enclosures. Figure 6 displays the isotherms and streamlines generated by our numerical code alongside those from Basak et al. [64] for a square cavity with porous media (Pr = 0.71, Ra = 10^6, Da = 10^{-5}). The excellent agreement between these results further substantiates the robustness of our computational framework.

The quantitative validation extended to heat transfer performance metrics, with Figure 7 depicting the local Nusselt number distribution along the horizontal coordinate at various Darcy numbers. The comparative analysis between our predictions and those of Basak et al. [64] reveals strong agreement across the entire range of permeability values, confirming the accuracy of our heat transfer calculations in porous media systems.

These multiple validation exercises collectively affirm the reliability of our numerical methodology for investigating MHD flow and heat transfer phenomena in the annular porous configurations examined in this study.

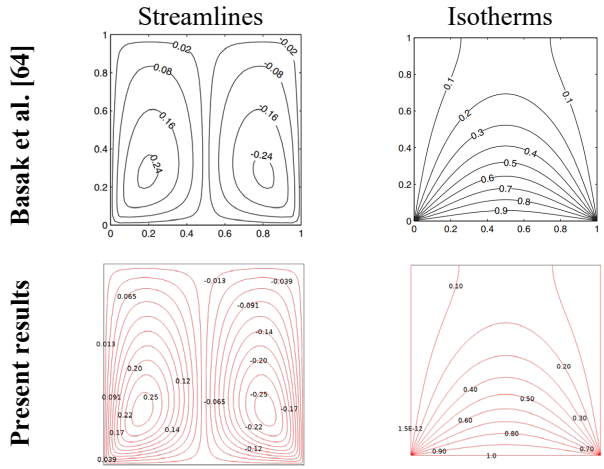

Figure 6. Comparison of isotherms and streamlines between the present study and Basak et al. [64] results

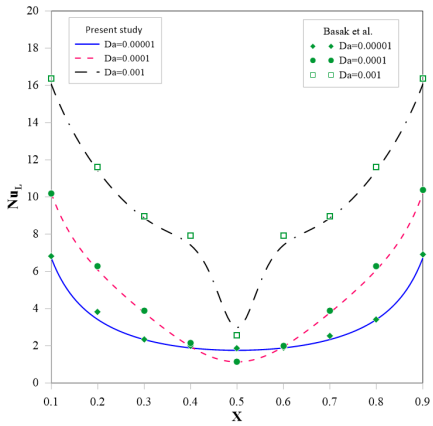

Figure 7. Local Nusselt number distribution comparison between the present study and Basak et al. [64] results

3. RESULTS AND DISCUSSION

3.1 Overview of the parametric study

This section presents the computational findings for MHD natural convection of the Ag–MgO/water hybrid nanofluid in the annular double-pipe heat exchanger described in Section 2. For clarity, the four porous-layer configurations examined throughout this study are briefly recalled: Case 1 consists of four equal 45° porous sectors distributed symmetrically; Case 2 comprises two 90° porous sectors arranged diagonally; Case 3 corresponds to a semicircular porous layer occupying the bottom half of the annulus; and Case 4 features a semicircular porous layer occupying the right half. These configurations are referred to consistently throughout the discussion without further geometric repetition.

The following subsections examine, in turn, the effects of

the Rayleigh number (Section 3.2), the Darcy number (Section 3.3), the magnetic-field orientation and strength (Section 3.4), and the coupled influence of radiation and nanoparticle loading (Section 3.5). A concluding synthesis of the principal findings is presented in Section 3.6.

3.2 Effect of Rayleigh number

Figure 8 presents the isothermal contours across the four different porous layer configurations (Cases 1-4) for varying Rayleigh numbers ($Ra = 10^3$ to 10^6) at fixed parameters ($Ha = 5$, $\gamma = 0$, $\varphi = 0.01$, $\lambda = 1$, $Rd = 1$). At low Rayleigh numbers ($Ra = 10^3$ and 10^4), all four configurations display nearly concentric isothermal patterns, indicating conduction-dominated heat transfer. The temperature gradients are steepest near the inner wall and gradually decrease toward the outer boundary, with minimal variation between the different porous arrangements. This uniformity confirms that, at low Ra values, thermal transport is primarily governed by conduction mechanisms, regardless of the porous media distribution. As the Rayleigh number increases to $Ra = 10^5$, the isothermal contours begin to show subtle distortions from perfect concentricity, particularly in Cases 2, 3, and 4. These distortions signify the emerging influence of natural convection as buoyancy forces start to overcome viscous forces. The symmetrical arrangement in Case 1 continues to maintain relatively concentric isothermal patterns due to its uniform distribution of flow resistance. At $Ra = 10^6$, dramatic changes appear in the isothermal patterns across all configurations. Case 1 develops plume-like distortions aligned with the four porous sections, indicating the formation of convective cells within the symmetrical structure. Case 2 exhibits pronounced thermal stratification with isotherms concentrated in the upper region, demonstrating strong buoyancy-driven flow. Case 3 shows distinct horizontal thermal stratification, characterised by compressed isotherms at the interface between the porous and clear fluid regions, indicating significant flow resistance at this boundary. Case 4 displays asymmetric thermal patterns with isotherms clustering near the vertical porous interface.

These distinct thermal patterns at high Ra values illustrate how the geometric arrangement of porous media critically influences flow circulation and thermal transport pathways when convection becomes dominant. The physical mechanism involves the interaction between buoyancy-driven flows and the localized flow resistance imposed by the porous regions, creating preferential circulation patterns unique to each configuration. These circulation patterns determine the overall heat transfer efficiency and explain the variations in Nusselt number observed across the different cases at high Rayleigh numbers.

Figure 9 illustrates the stream function contours for the four porous layer configurations across varying Rayleigh numbers ($Ra = 10^3$ to 10^6) at fixed parameters ($Ha = 5$, $\gamma = 0$, $\varphi = 0.01$, $\lambda = 1$, $Rd = 1$).

At $Ra = 10^3$, all configurations exhibit a similar bipolar circulation pattern with two primary vortices - a clockwise vortex (blue region) on the left and a counterclockwise vortex (red/orange region) on the right. This pattern indicates that even at low Ra, natural convection establishes a basic flow structure driven by buoyancy forces. Case 4 shows a noticeably stronger circulation intensity due to its half-vertical porous arrangement, which offers less resistance to the primary convection pattern. As Ra increases to 10^4 and 10^5, the fundamental bipolar structure persists across all configurations, but with gradually increasing circulation intensity. The stream function contours become more compressed, indicating stronger velocity gradients and enhanced convective flow. Case 3 (bottom-half porous configuration) demonstrates the weakest circulation intensity, as the horizontal porous layer impedes the natural vertical buoyancy-driven flow.

At $Ra = 10^6$, significant differences emerge between the cases. Case 3 undergoes significant flow restructuring, developing multiple smaller vortices that indicate flow instability and potential transition to a turbulent regime. Cases 1, 2, and 4 maintain their bipolar structure but with varying intensities and distributions. Case 4 continues to exhibit the strongest circulation, while Case 2 shows some weakening of the primary vortices. The physical mechanism underlying these patterns involves the competing effects of buoyancy forces (which drive circulation) and the localized flow resistance imposed by the porous regions. The spatial arrangement of porous media creates preferential flow pathways that either facilitate or impede the natural convection cells. As Ra increases, the intensified buoyancy forces overwhelm the flow resistance in certain configurations (particularly Case 3), leading to flow instabilities and reorganization of the circulation patterns. These distinct flow structures directly influence the heat transfer performance and explain the variations in thermal transport efficiency observed across the different porous arrangements at high Rayleigh numbers.

Figure 10 illustrates the effect of Rayleigh number (Ra) on the average Nusselt number (Nu_{av}), total entropy generation (S_{total}), and Bejan number (Be) across the four different porous layer configurations at fixed parameters ($Ha = 5$, $\gamma = 0$, $\varphi = 0.01$, $\lambda = 1$, $Rd = 1$).

The average Nusselt number data reveal distinctive thermal performance trends across the configurations. For Case 1 (four symmetrical porous sections), Nu_{av} increases modestly from 19.702 to 21.722 as Ra rises from 10^3 to 10^6, representing a 10.25% enhancement. Case 2 (diagonal porous arrangement) exhibits the most dramatic improvement, with Nu_{av} increasing from 17.846 to 23.11, marking a 29.50% growth at higher Ra values. Conversely, Case 3 (bottom-half porous layer) shows a declining trend, with Nu_{av} decreasing by 20.28% from 15.047 to 11.996 as Ra increases. Case 4 (right-half porous configuration) demonstrates moderate enhancement, with Nu_{av} rising from 15.067 to 16.334 (8.41% increase).

These variations can be attributed to the interplay between buoyancy-driven flow and the distribution of porous media. As Ra increases, the dominance of buoyancy forces intensifies natural convection, but the spatial arrangement of porous regions critically influences flow circulation patterns. The diagonal arrangement in Case 2 appears to facilitate optimal flow circulation at higher Ra values, creating efficient thermal pathways that enhance convective heat transfer. Conversely, the horizontal porous layer in Case 3 increasingly obstructs the natural buoyancy-driven flow as Ra increases, impeding thermal transport.

Regarding entropy generation, all configurations exhibit dramatic increases with rising Ra, reflecting intensified irreversibilities at higher convection regimes. The most pronounced increase occurs in Case 4, where S_{total} escalates from 5.6513 at $Ra = 10^3$ to 15,592 at $Ra = 10^6$, representing approximately 2,760 times greater entropy generation. This substantial growth indicates that the half-vertical porous arrangement magnifies fluid friction and thermal gradients at

high Ra values. Case 3, despite its declining heat transfer performance, generates significant entropy (14,112 at Ra = 10^6), suggesting considerable thermal mixing and flow resistance across the horizontal porous interface.

The Bejan number analysis provides insight into the relative contributions of thermal and viscous irreversibilities. For all configurations, Be decreases markedly as Ra increases, indicating that fluid friction increasingly dominates over thermal gradients at higher Ra values. This transition is most dramatic in Case 4, where Be decreases sharply from 0.99092 to 0.0028187 (99.72% reduction), signifying that fluid friction becomes the overwhelming irreversibility source. Case 3 maintains the highest Be values at high Ra (Ra = 10^6), which is 0.069536, suggesting that thermal irreversibility remains more significant in this configuration despite its lower heat transfer performance. From a second-law perspective, the Bejan number can be expressed as:

$$Be = S_{gen,thermal} / (S_{gen,thermal} + S_{gen,viscous})$$

where, the thermal contribution scales with $(\nabla\theta)^2$ while the viscous contribution scales with the squared velocity gradients $(\partial U/\partial X)^2$, $(\partial V/\partial Y)^2$, and $(\partial U/\partial Y + \partial V/\partial X)^2$. The extreme reduction of Be observed in Case 4 at Ra = 10^6 (Be ≈ 0.003) is therefore a direct fingerprint of the flow structure induced by the right-half porous arrangement. In this configuration, the strong buoyancy-driven circulation is forced to concentrate almost entirely within the non-porous half of the annulus, producing a localised high-velocity stream adjacent to the vertical fluid–porous interface. The resulting sharp velocity gradients and intense vorticity at this interface amplify the viscous irreversibility term by several orders of magnitude, whereas the thermal gradients remain comparable to those of the other configurations. Consequently, the viscous contribution dominates over the thermal one by a factor of nearly 350, driving Be toward zero. In contrast, Case 3 retains the highest Be values (≈0.07) because its horizontal porous layer obstructs the primary buoyancy-driven circulation, keeping velocity gradients modest while thermal stratification across the interface sustains the thermal irreversibility component. This interpretation, based on the local balance between velocity-gradient and temperature-gradient fields, provides a unified physical explanation for the contrasting Be trends observed across the four configurations and at different Rayleigh numbers.

These findings demonstrate that the geometric arrangement of porous media in annular heat exchangers substantially influences both heat transfer performance and thermodynamic irreversibilities, with diagonal porous arrangements (Case 2) offering superior thermal enhancement at high Ra values while vertical partitioning (Case 4) generates the greatest overall entropy.

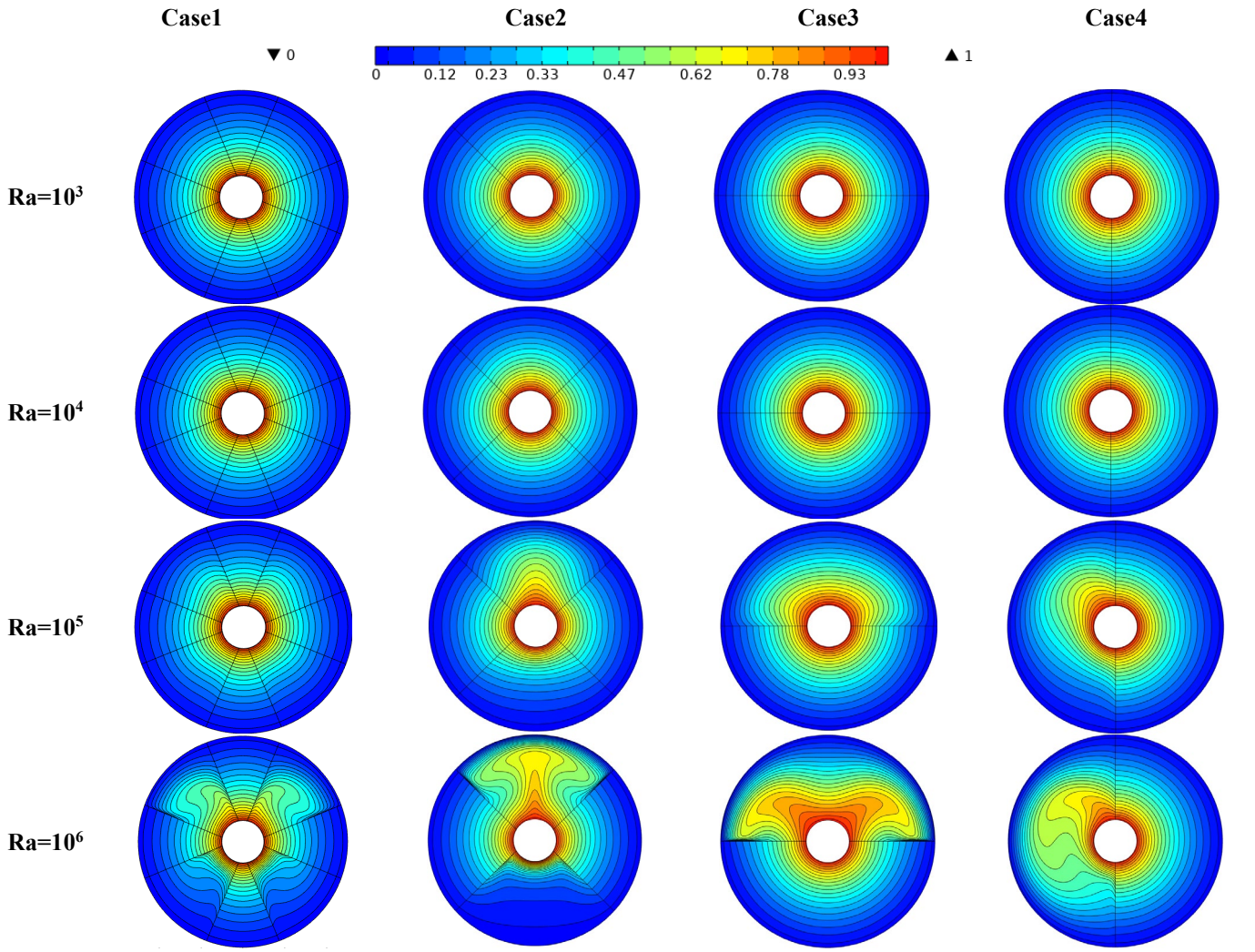

Figure 8. Isothermal contours at different values of Rayleigh number for different configurations at Ha = 5, γ = 0, φ = 0.01, λ = 1, Rd = 1

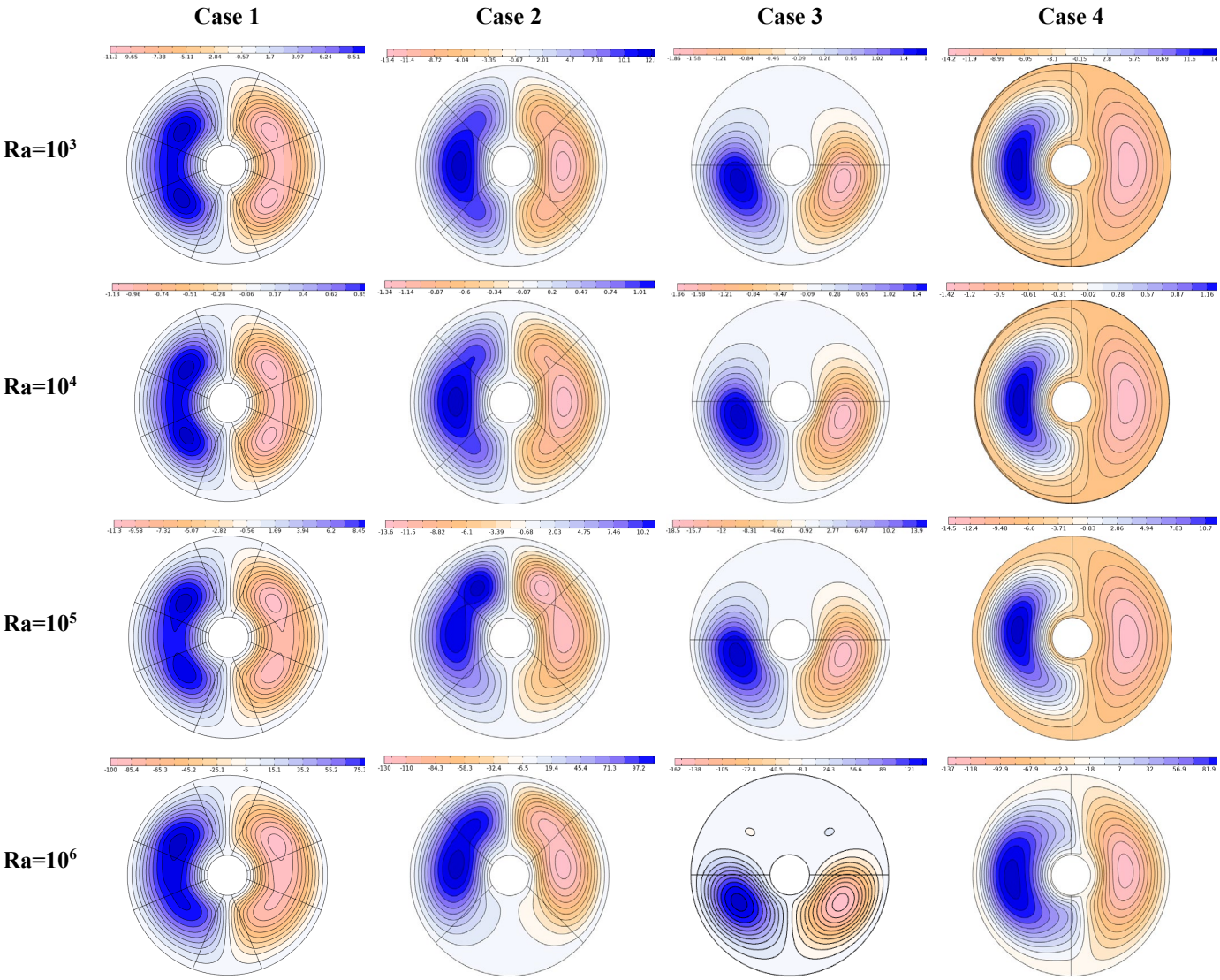

Figure 9. Stream function contours at different values of Rayleigh number for different configurations at Ha = 5, $\gamma = 0$, $\varphi = 0.01$, $\lambda = 1$, Rd = 1

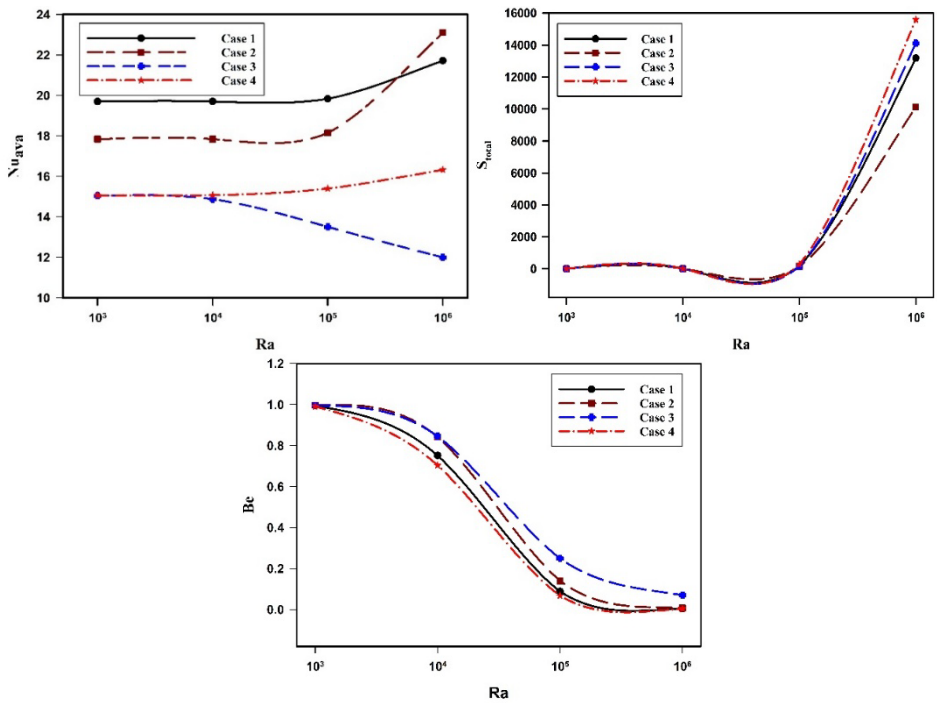

Figure 10. Effect of Rayleigh number for different cases on Nu_{av}, S_{total}, and Be for Ha = 5, $\gamma = 0$, $\varphi = 0.01$, $\lambda = 1$, Rd = 1

3.3 Effect of Darcy number

Figure 11 displays the isothermal contours for the four porous layer configurations across varying Darcy numbers (Da = 10^{-5} to 10^{-2}) at fixed parameters (Ra = 10^5, Ha = 5, $\gamma = 0$, $\varphi = 0.01$, $\lambda = 1$, Rd = 1).

At low Darcy numbers (Da = 10^{-5} and 10^{-4}), all four configurations exhibit nearly concentric isothermal patterns, indicating conduction-dominated heat transfer. The low permeability of the porous media at these Da values significantly restricts fluid movement, forcing heat transfer to occur primarily through conduction regardless of the porous layer arrangement. Minor deviations from perfect concentricity are evident in Cases 3 and 4, reflecting the influence of their asymmetric porous distributions.

As the Darcy number increases to Da = 10^{-3}, subtle changes begin to appear in the isothermal patterns. The contours in Cases 2, 3, and 4 exhibit slight distortions, indicating the emergence of convective effects as increased permeability allows for more fluid circulation within the porous regions. Case 1 maintains relatively concentric patterns due to its symmetrical porous distribution, resulting in balanced flow resistance in all directions.

At Da = 10^{-2}, more pronounced distortions appear in the isothermal contours, especially in Cases 3 and 4. Case 3 exhibits horizontal elongation of the isotherms in the upper non-porous region, while Case 4 shows asymmetric thermal patterns with isotherms clustering near the vertical porous interface. These distortions signify enhanced convective transport as the higher permeability reduces flow resistance within the porous media.

The physical mechanism underlying these patterns involves the balance between viscous forces and inertial effects within the porous media. As Da increases, the Darcy-Forchheimer flow resistance decreases, allowing for more vigorous fluid circulation and, consequently, enhanced convective heat transfer. The spatial arrangement of the porous regions determines preferential flow pathways, which in turn shapes the temperature distribution. The relative persistence of near-concentric patterns across all Da values indicates that at Ra = 10^5, the porous media configuration exerts greater influence on heat transfer patterns than permeability variations, suggesting that geometric optimization may be more effective than permeability modulation for enhancing thermal performance in these systems.

Figure 12 illustrates the stream function contours for the four porous layer configurations across varying Darcy numbers (Da = 10^{-5} to 10^{-2}) at fixed parameters (Ra = 10^5, Ha = 5, $\gamma = 0$, $\varphi = 0.01$, $\lambda = 1$, Rd = 1).

At Da = 10^{-5}, all four cases display distinct flow patterns that are strongly influenced by their porous media distributions. Case 1 exhibits four pairs of counter-rotating vortices aligned with the porous sections, while Case 2 shows four smaller vortices confined primarily to the non-porous regions. Case 3 demonstrates a single pair of elongated vortices constrained by the horizontal porous layer, and Case 4 features highly asymmetric circulation with intense flow restricted to the non-porous half.

As Da increases to 10^{-4}, vortex structures begin to expand as the reduced flow resistance allows greater penetration into the porous regions. The flow patterns remain similar to those at Da = 10^{-5}, but with modestly increased circulation intensity, particularly visible in Cases 2 and 4.

At Da = 10^{-3}, significant flow restructuring occurs. Cases 1 and 2 evolve toward more conventional bipolar circulation patterns, characterised by two dominant counter-rotating vortices, indicating that the porous regions no longer severely restrict flow. Case 3 maintains its horizontal stratification but with enhanced circulation strength, while Case 4 develops a more balanced bilateral flow structure.

By Da = 10^{-2}, all configurations converge toward similar bipolar circulation patterns, while still preserving characteristics influenced by their specific porous arrangements. Case 1 retains slightly distorted vortices aligned with the porous sections, while Cases 3 and 4 show asymmetric intensity distributions reflecting their non-uniform porous media distribution.

The physical mechanism underlying these transitions involves the progressive dominance of inertial forces over Darcy resistance as permeability increases. At low Da values, flow is heavily constrained by the porous media, creating fragmented circulation patterns dictated by the geometric arrangement of flow obstacles. As Da increases, the diminished flow resistance allows buoyancy-driven convection to establish more natural circulation patterns characteristic of non-porous enclosures. This transition explains the convergence toward similar flow structures at high Da values, where the influence of porous media arrangement becomes secondary to the fundamental convective mechanism driven by the temperature gradient between the inner and outer walls.

Figure 13 demonstrates the influence of Darcy number (Da) on the average Nusselt number (Nu_{av}), total entropy generation (S_{total}), and Bejan number (Be) for the four different porous layer arrangements at fixed parameters (Ra = 10^5, Ha = 5, $\gamma = 0$, $\varphi = 0.01$, $\lambda = 1$, Rd = 1).

The average Nusselt number analysis reveals contrasting trends across the configurations as Da increases from 10^{-5} to 10^{-2}. In Cases 1 and 2 (symmetrical and diagonal porous arrangements), Nu_{av} shows modest increases of 0.96% (19.744 to 19.933) and 4.63% (17.872 to 18.699), respectively. Conversely, Cases 3 and 4 exhibit decreasing heat transfer performance, with Nu_{av} reductions of 14.10% (15.014 to 12.897) and 12.02% (16.638 to 14.638). This behavior indicates that increased permeability within the porous media (higher Da) enhances convective transport in symmetrical configurations while degrading performance in asymmetrical arrangements.

The physical explanation for these trends lies in the interaction between fluid momentum and the resistance of the porous medium. As Da increases, fluid can penetrate more easily through the porous regions, altering flow patterns. In Cases 1 and 2, this enhanced permeability facilitates fluid circulation and improves convective heat transfer. However, in Cases 3 and 4, higher permeability disrupts the established buoyancy-driven circulation patterns, leading to less efficient thermal transport pathways and reduced heat transfer effectiveness.

Total entropy generation exhibits a dramatic increase with rising Da values across all configurations, indicating intensified irreversibilities at higher permeabilities. The most substantial increase occurs in Case 3, where S_{total} escalates from 5.821 at Da = 10^{-5} to 894.3 at Da = 10^{-2}, representing a remarkable 15,263% increase. Case 4 maintains the highest absolute entropy generation values, reaching 962.79 at Da = 10^{-2}, suggesting that the half-vertical porous arrangement creates significant thermodynamic irreversibilities. This substantial entropy generation stems from intensified mixing

and flow interactions at the clear fluid-porous media interfaces, which become more pronounced at higher permeabilities.

The Bejan number analysis provides crucial insight into the dominant irreversibility mechanisms. All configurations show decreasing Be values with increasing Da, indicating that fluid friction irreversibilities progressively dominate over thermal irreversibilities as permeability increases. Case 3 maintains the highest Be values across all Da ranges (from 0.98435 to 0.18136), suggesting that thermal irreversibilities remain relatively more significant in the horizontal porous layer configuration. Conversely, Case 4 experiences the lowest Be values at high Da (0.028293 at Da = 10^{-2}), indicating that fluid friction becomes overwhelmingly dominant in the vertical porous arrangement.

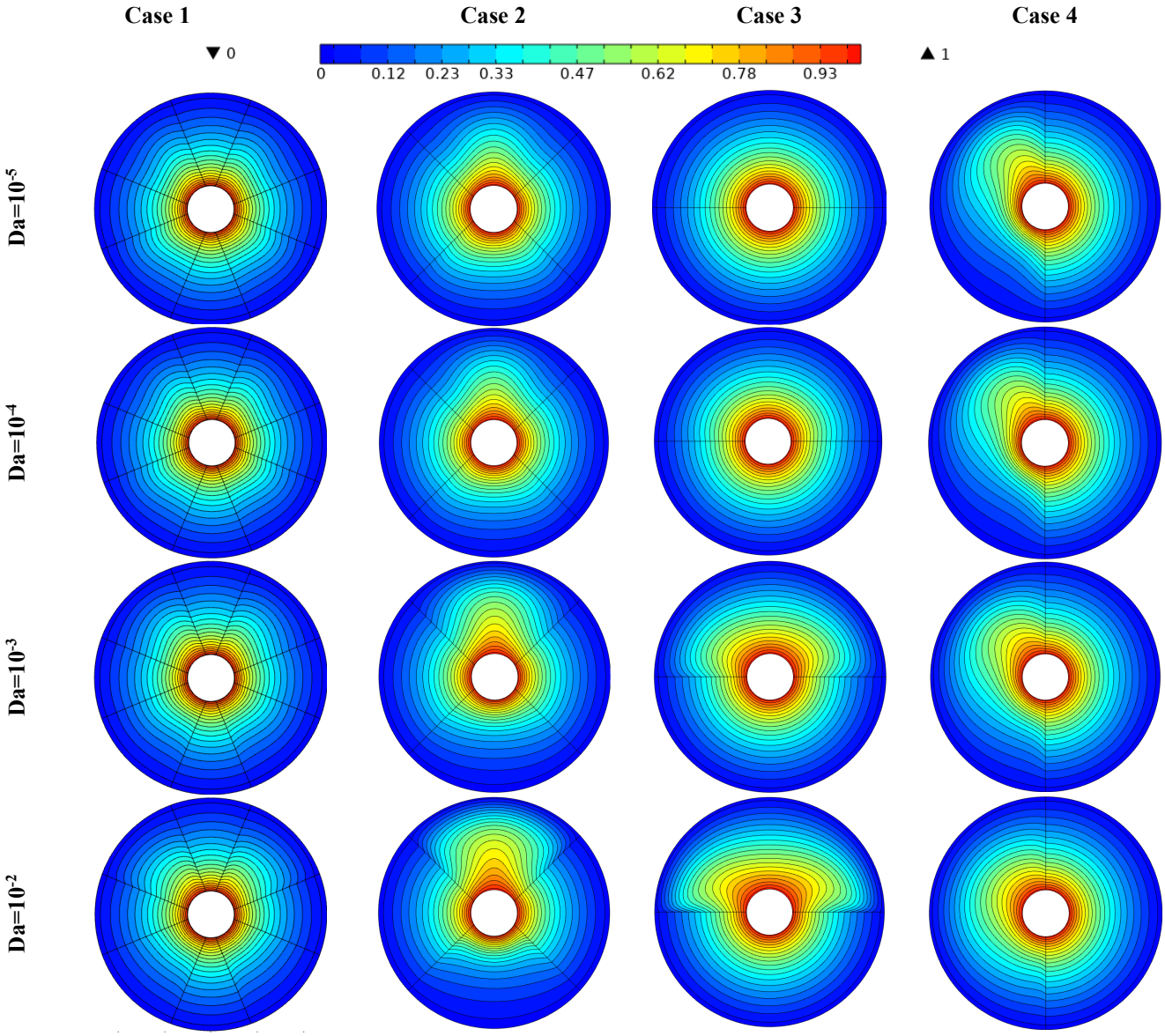

Figure 11. Isothermal contours at different values of Darcy number for different configurations at Ra = 10^5, Ha = 5, γ = 0, φ = 0.01, λ = 1, Rd = 1

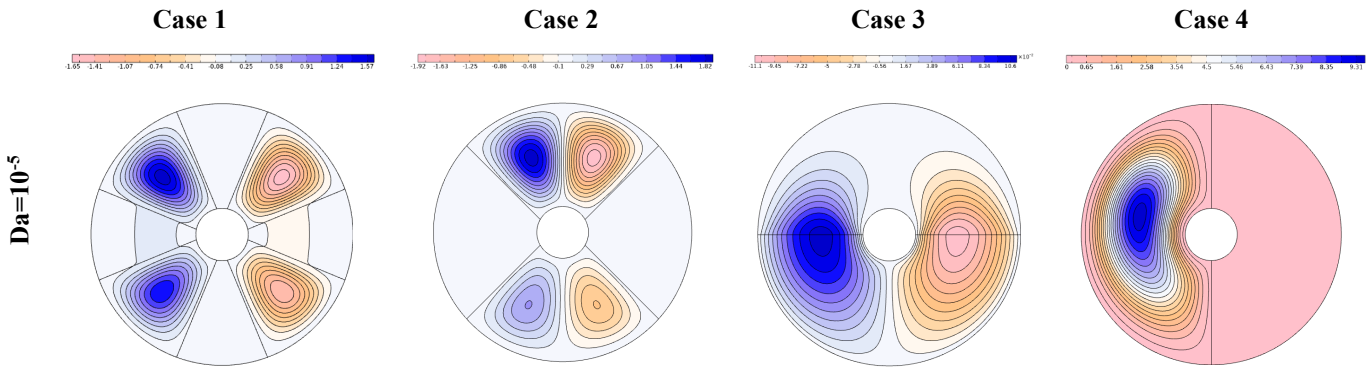

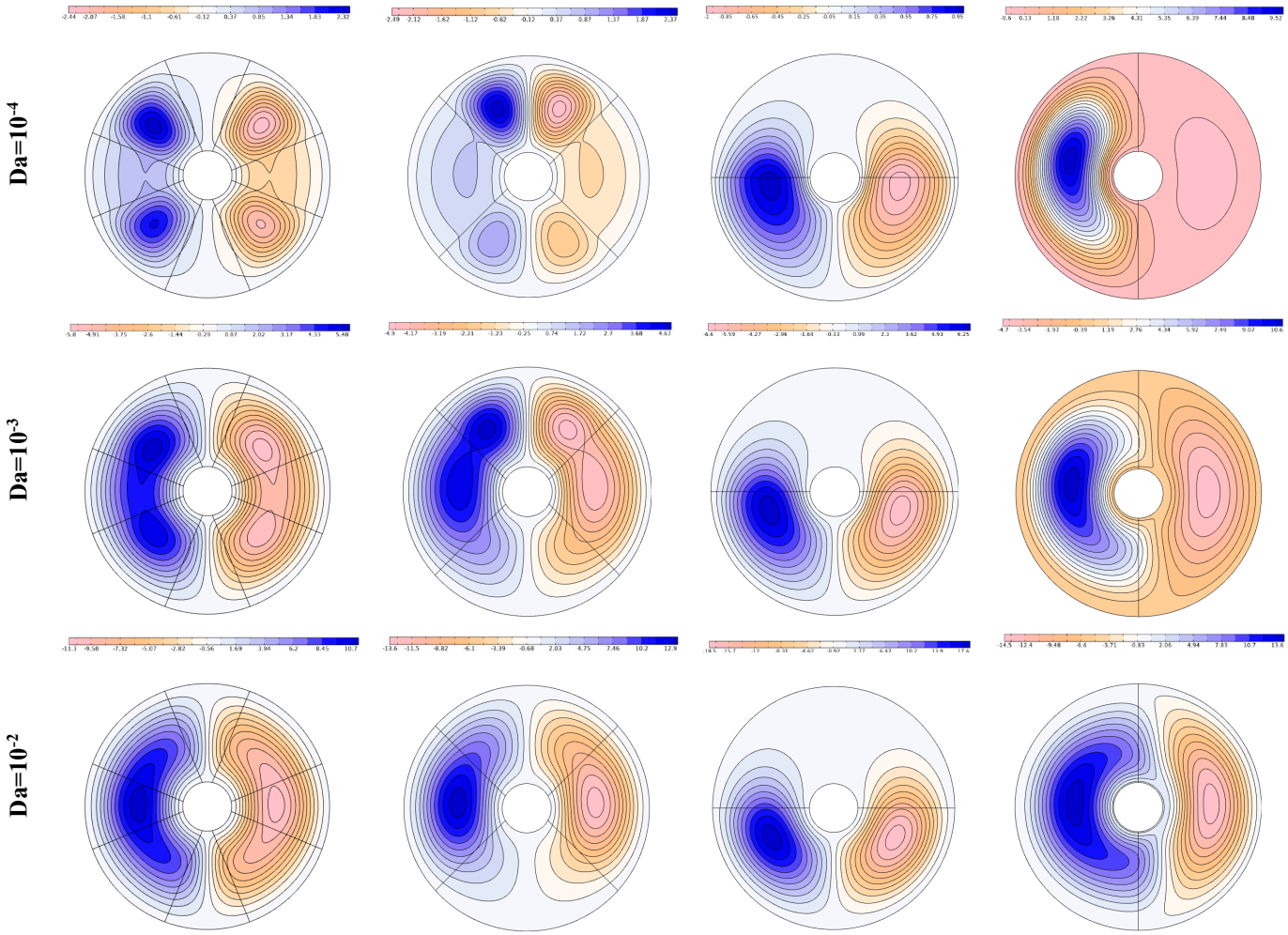

Figure 12. Stream function contours at different values of Darcy number for different configurations at Ra = 10^5, Ha = 5, γ = 0, φ = 0.01, λ = 1, Rd = 1

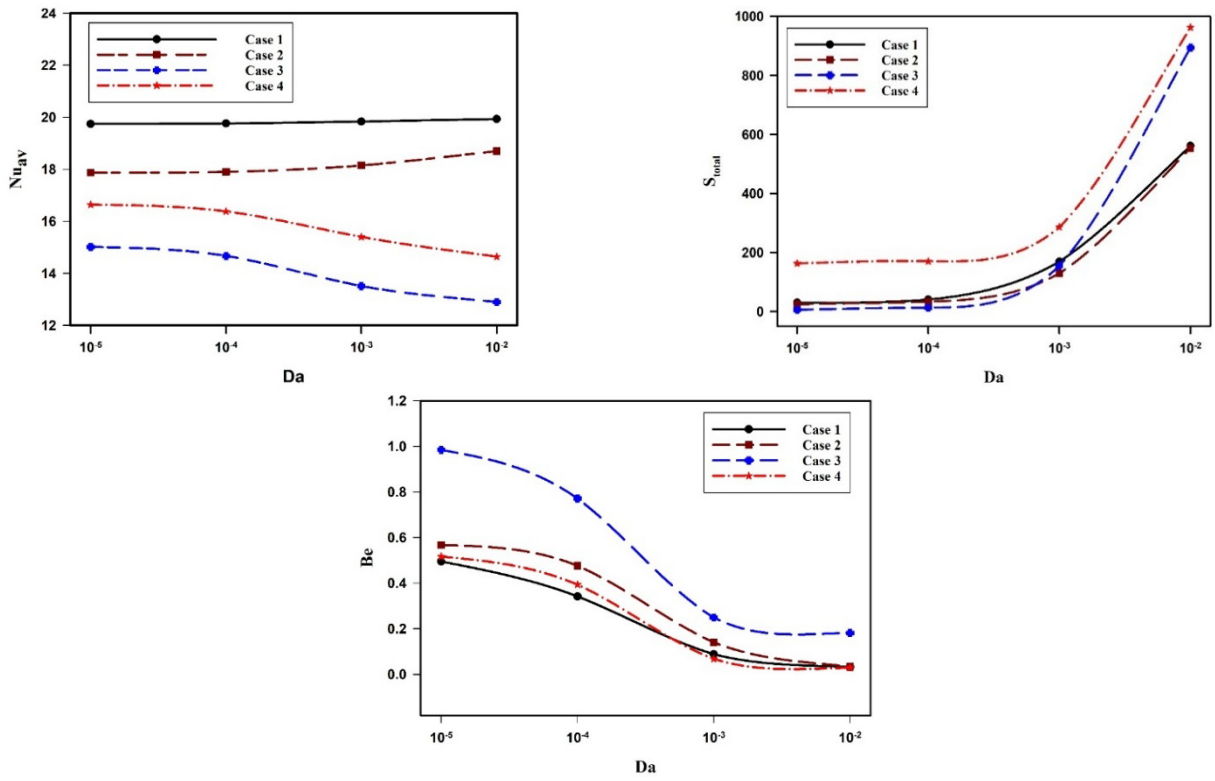

Figure 13. Effect of Darcy number for different cases on Nu_{av}, S_{total}, and Be for Ra = 10^5, Ha = 5, γ = 0, φ = 0.01, λ = 1, Rd = 1

3.4 Effect of magnetic field

These findings demonstrate that permeability modulation through the Darcy number has a significant impact on both heat transfer performance and thermodynamic efficiency in annular heat exchangers with porous media. The results highlight that symmetrical porous arrangements offer more robust thermal performance across permeability ranges, while the entropy generation patterns reveal complex fluid-thermal interactions that must be carefully balanced when designing such systems for practical engineering applications.

Figure 14 displays the isothermal contours for the four porous layer configurations across varying magnetic field angles ($\gamma = 0°$ to $90°$) at fixed parameters ($Ra = 10^5$, $Ha = 5$, $Da = 10^{-3}$, $\varphi = 0.01$, $\lambda = 1$, $Rd = 1$).

The most striking observation is the remarkable similarity of isothermal patterns across all magnetic field orientations for each respective configuration. For all cases, the temperature contours remain nearly identical as γ increases from 0° to 90°, indicating minimal influence of magnetic field orientation on the temperature distribution within the annular domain.

This thermal field stability can be explained by the moderate Hartmann number ($Ha = 5$) employed in this analysis. At this magnetic field strength, the Lorentz force is present but not sufficiently strong to reorganise the temperature field significantly. The primary heat transfer mechanisms—conduction through the porous media and convection in the fluid regions—maintain their dominance over MHD effects regardless of field orientation.

Each configuration maintains its distinctive thermal signature across all magnetic field angles: Case 1 exhibits near-concentric isotherms with slight distortions aligned with the symmetrical porous sections; Case 2 shows more pronounced distortions in the diagonal directions; Case 3 displays horizontal elongation of isotherms in the clear fluid region; and Case 4 demonstrates asymmetric thermal patterns with isotherms clustering near the vertical porous interface.

The physical explanation for this insensitivity to magnetic field angle lies in the complex interaction between the flow of porous media resistance and electromagnetic forces. At $Ra = 10^5$ and $Da = 10^{-3}$, the flow structure is predominantly determined by buoyancy forces and porous media distribution. The magnetic field at $Ha = 5$ imposes a secondary influence that, while affecting flow velocities and patterns (as seen in streamline variations), is insufficient to reorganise the temperature field significantly. The results suggest that at these parameter values, thermal optimization strategies should focus on porous media configuration rather than magnetic field orientation adjustments.

Figure 15 depicts the stream function contours for the four porous layer configurations across varying magnetic field angles ($\gamma = 0°$ to $90°$) at fixed parameters ($Ra = 10^5$, $Ha = 5$, $Da = 10^{-3}$, $\varphi = 0.01$, $\lambda = 1$, $Rd = 1$).

Similar to the thermal field observations, the flow patterns exhibit remarkable consistency across all magnetic field orientations. All four configurations maintain their characteristic flow structures as γ increases from 0° to 90°, with only subtle variations in vortex intensity and positioning. Cases 1 and 2 maintain bipolar circulation with clockwise (blue) and counterclockwise (red) vortices on opposite sides, Case 3 displays horizontally elongated vortices, and Case 4 shows asymmetric circulation concentrated in the non-porous region.

The relative insensitivity of flow patterns to magnetic field orientation can be attributed to several interacting physical mechanisms. At $Ha = 5$, the magnetic field introduces moderate Lorentz forces that influence but do not dominate the flow dynamics. The primary driving forces remain buoyancy (from temperature differences) and flow resistance from the porous media. As the magnetic field rotates, the Lorentz force components change direction, but their magnitude remains insufficient to reorganize the established circulation patterns dictated by the geometric arrangement of porous regions.

The modest variations observed include slight adjustments in vortex intensity and subtle shifts in vortex positioning, particularly visible in Cases 2 and 3. These minor changes reflect the reorientation of electromagnetic damping forces as the field angle changes, selectively suppressing velocity components perpendicular to the field direction.

This flow stability across magnetic field orientations explains the corresponding stability observed in the temperature fields and heat transfer metrics. The results suggest that at moderate Hartmann numbers ($Ha = 5$), the porous media configuration plays a far more decisive role in determining flow structure and thermal performance than magnetic field orientation. For engineering applications seeking to optimize such systems, these findings indicate that geometric optimization of porous media distribution would yield more significant performance improvements than adjustments to magnetic field orientation.

Figure 16 illustrates the effect of magnetic field orientation angle (γ) on the average Nusselt number (Nu_{av}), total entropy generation (S_{total}), and Bejan number (Be) for the four different porous layer configurations at fixed parameters ($Ra = 10^5$, $Da = 10^{-3}$, $\varphi = 0.01$, $\lambda = 1$, $Rd = 1$).

The average Nusselt number data reveal minimal variation across all configurations as the magnetic field angle increases from 0° to 90°. Case 1 (symmetrical porous sections) shows a negligible increase of only 0.01% in Nu_{av} (from 19.837 to 19.839), while Case 2 (diagonal arrangement) exhibits a slight increase of 0.06% (from 18.151 to 18.161). Interestingly, Case 3 (bottom-half porous layer) demonstrates a minor decrease of 0.21% (from 13.507 to 13.478), whereas Case 4 (right-half configuration) shows a non-monotonic trend, initially increasing by 0.46% as γ rises from 0° to 60° (15.396 to 15.467) before decreasing slightly at $\gamma = 90°$ (15.447).

This limited influence of magnetic field orientation on heat transfer performance can be attributed to the dominant effect of the porous structure and buoyancy forces at the given Rayleigh number. The MHD effects, while present, are insufficient to significantly alter the established flow patterns determined by the geometric arrangement of the porous media. The slight variations observed suggest that the Lorentz force component changes with field orientation, marginally modifying the flow structure within the annular region.

Total entropy generation shows a more pronounced response to magnetic field angle variations, with consistent increases across all configurations. Case 4 exhibits the most significant absolute increase, with S_{total} rising from 285.76 at $\gamma = 0°$ to 295.97 at $\gamma = 90°$ (3.57% increase). Similarly, Cases 1, 2, and 3 show increases of 2.57%, 2.74%, and 2.86%, respectively. This progressive rise in entropy generation reflects the increasing contribution of magnetic field-induced irreversibilities as the orientation changes. When the magnetic field aligns perpendicularly to the gravitational force ($\gamma = 90°$), it maximizes the disruption to the buoyancy-driven flow, leading to enhanced dissipation and entropy production.

The Bejan number analysis reveals a consistent decreasing

trend with increasing magnetic field angle across all configurations. Case a maintains the highest absolute Be values (ranging from 0.24866 to 0.24515), indicating that thermal irreversibilities remain relatively more significant in this configuration regardless of field orientation. The modest decrease in Be (approximately 1.41% across all cases) suggests that as the magnetic field angle increases, fluid friction irreversibilities become slightly more dominant compared to thermal irreversibilities.

These findings demonstrate that while magnetic field orientation has a limited impact on overall heat transfer performance in porous annular heat exchangers at the given parameters, it noticeably influences thermodynamic irreversibilities. The results highlight that the geometric distribution of porous media remains the primary determinant of thermal performance, with MHD effects serving as a secondary influence that primarily affects entropy generation characteristics rather than heat transfer efficiency. This insight is valuable for the design optimization of MHD heat exchangers, where thermodynamic efficiency considerations are paramount alongside thermal performance targets.

Figure 17 depicts the isothermal contours for the four porous layer configurations across varying Hartmann numbers (Ha = 0 to 50) at fixed parameters ($Ra = 10^5$, $\gamma = 0$, $Da = 10^{-3}$, $\varphi = 0.01$, $\lambda = 1$, $Rd = 1$).

As the Hartmann number increases from 0 to 50, a progressive transformation toward more concentric isothermal patterns is observed across all configurations. At Ha = 0 (no magnetic field), each case exhibits characteristic thermal distortions reflecting its specific porous arrangements. Cases 3 and 4 show the most pronounced non-concentric patterns, with horizontal and vertical asymmetry, respectively.

With increasing magnetic field strength, these distortions gradually diminish. By Ha = 50, all configurations display nearly concentric isothermal contours, though subtle influences of the underlying porous structure remain visible. This transition is most dramatic in Cases 3 and 4, where the initially asymmetric patterns evolve toward axisymmetric distributions.

The physical mechanism behind this phenomenon is the electromagnetic dampening effect on fluid motion. As Ha increases, the Lorentz force progressively suppresses convective circulation, particularly in directions perpendicular to the magnetic field. This suppression reduces convective heat transfer, shifting the thermal transport mechanism toward conduction dominance. Since conductive heat transfer in a cylindrical geometry naturally produces concentric isothermal patterns, the temperature distribution increasingly approaches this ideal form as convection is inhibited.

This transition explains the observed trends in Nusselt number, where Cases 1 and 2 showed declining heat transfer performance with increasing Ha, while Case 3 exhibited enhanced performance. The initially inefficient thermal transport in Case 3 (with its horizontal porous layer obstructing natural convection) becomes relatively more effective as the magnetic field suppresses convection in all configurations, leading to its comparative advantage at high Ha values.

These results demonstrate that magnetic field strength can serve as an effective mechanism for controlling and homogenizing temperature distributions in porous annular heat exchangers, with the potential to either enhance or diminish thermal performance depending on the specific porous media configuration.

Figure 18 presents the stream function contours for the four porous layer configurations across varying Hartmann numbers (Ha = 0 to 50) at fixed parameters ($Ra = 10^5$, $\gamma = 0$, $Da = 10^{-3}$, $\varphi = 0.01$, $\lambda = 1$, $Rd = 1$). As the Hartmann number increases from 0 to 50, a consistent and progressive weakening of flow circulation is observed across all configurations. At Ha = 0 (no magnetic field), each case exhibits robust bipolar circulation patterns with clockwise (blue) and counterclockwise (red) vortices, though with distinctive characteristics reflecting their porous media distribution.

With increasing magnetic field strength, the circulation intensity diminishes substantially, as evidenced by the reduced density and expanded spacing of stream function contours. By Ha = 50, all configurations display significantly weakened flow structures, though the fundamental bipolar pattern persists. This weakening is particularly evident in Case 3, where the vortices become notably diffuse at high Ha values. The physical mechanism responsible for this behavior is the electromagnetic braking effect. As Ha increases, the Lorentz force (proportional to Ha^2) exerts growing resistance against fluid motion perpendicular to the magnetic field direction. This electromagnetic damping creates additional flow resistance beyond that imposed by the porous media, effectively suppressing convective circulation.

Despite the overall weakening trend, each configuration maintains its characteristic flow structure, indicating that the geometric arrangement of porous media continues to influence flow patterns even under strong magnetic conditions. Case 4 appears to retain relatively stronger circulation at high Ha values compared to the other configurations, suggesting some resistance to electromagnetic suppression.

This progressive flow suppression explains the corresponding evolution toward conduction-dominated heat transfer observed in the isothermal patterns, as well as the significant reduction in entropy generation with increasing Ha. The results demonstrate that magnetic field strength serves as an effective mechanism for controlling flow intensity in porous annular heat exchangers, with implications for both thermal performance and pumping power requirements in practical applications.

Figure 19 demonstrates the influence of Hartmann number (Ha) on the average Nusselt number (Nu_{av}), total entropy generation (S_{total}), and Bejan number (Be) across the four porous layer configurations at fixed parameters ($Ra = 10^5$, $Da = 10^{-3}$, $\gamma = 0$, $\varphi = 0.01$, $\lambda = 1$, $Rd = 1$).

The average Nusselt number analysis reveals distinctive trends as Ha increases from 0 to 50. Cases 1 and 2 exhibit gradual decreases in heat transfer performance, with Nu_{av} declining by 0.67% (from 19.846 to 19.713) and 1.78% (from 18.178 to 17.855), respectively. In striking contrast, Case 3 shows a significant enhancement in heat transfer, with Nu_{av} increasing by 7.56% (from 13.479 to 14.498). Case 4 demonstrates a non-monotonic behavior, initially decreasing by 2.87% as Ha increases from 0 to 30 (15.456 to 15.013), before slightly recovering at Ha = 50 (15.037). This divergent behavior highlights the complex interaction between the magnetic field strength and the distribution of porous media.

The physical mechanism underlying these trends can be attributed to the Lorentz force induced by the magnetic field, which suppresses convective motion perpendicular to the field direction. In Cases 1 and 2, this suppression inhibits the established convective patterns, reducing heat transfer efficiency. Conversely, in Case 3 (bottom-half porous configuration), the magnetic field appears to reorganize flow

structures in a manner that enhances thermal transport, possibly by creating more efficient circulation patterns that overcome the inherent limitations of the horizontal porous arrangement.

Total entropy generation exhibits a remarkable non-monotonic trend across all configurations. Initially, S_{total} decreases as Ha increases from 0 to 30, with reductions of 66.35%, 66.60%, 63.50%, and 73.31% for Cases 1-4, respectively. The response of total entropy generation to the Hartmann number is distinctly non-monotonic. As Ha increases from 0 to 30, S_{total} decreases markedly by 66.4%, 66.6%, 63.5%, and 73.3% for Cases 1–4, respectively, reflecting the progressive suppression of fluid-friction irreversibilities by the Lorentz force. Beyond this minimum, S_{total} rises again as Ha further increases to 50, indicating that electromagnetic (Joule-type) dissipation begins to overtake the fluid-friction reduction gained from flow damping. The values at Ha = 50 nonetheless remain below those at Ha = 0, so that the net effect of moderate-to-strong magnetic fields is still beneficial from a second-law perspective, with the optimum located near Ha ≈ 30. This behavior indicates that moderate magnetic field strengths (up to Ha = 30) suppress flow-induced irreversibilities, while stronger fields (Ha = 50) introduce additional electromagnetic dissipation that contributes to entropy generation.

The Bejan number analysis reveals a consistent increase with rising Ha values across all configurations, indicating a progressive shift in the dominant irreversibility mechanism. Case 3 maintains the highest Be values throughout (increasing from 0.2444 to 0.57664), suggesting that thermal irreversibilities remain relatively more significant in this configuration. The substantial increase in Be (approximately 420-540% across all cases) as Ha rises from 0 to 50 demonstrates that magnetic field-induced suppression of fluid motion substantially reduces fluid friction irreversibilities relative to thermal irreversibilities.

These findings emphasize that magnetic field strength serves as a critical control parameter for both heat transfer performance and thermodynamic irreversibilities in porous annular heat exchangers. The results highlight that different porous media configurations respond uniquely to magnetic field influence, with horizontal porous arrangements (Case 3) benefiting from increased field strength, while symmetrical and diagonal configurations experience modest performance degradation. This insight provides valuable guidance for the design optimization of MHD heat exchangers, suggesting that porous media distribution should be tailored to the anticipated magnetic field conditions to maximize thermal performance while managing thermodynamic irreversibilities.

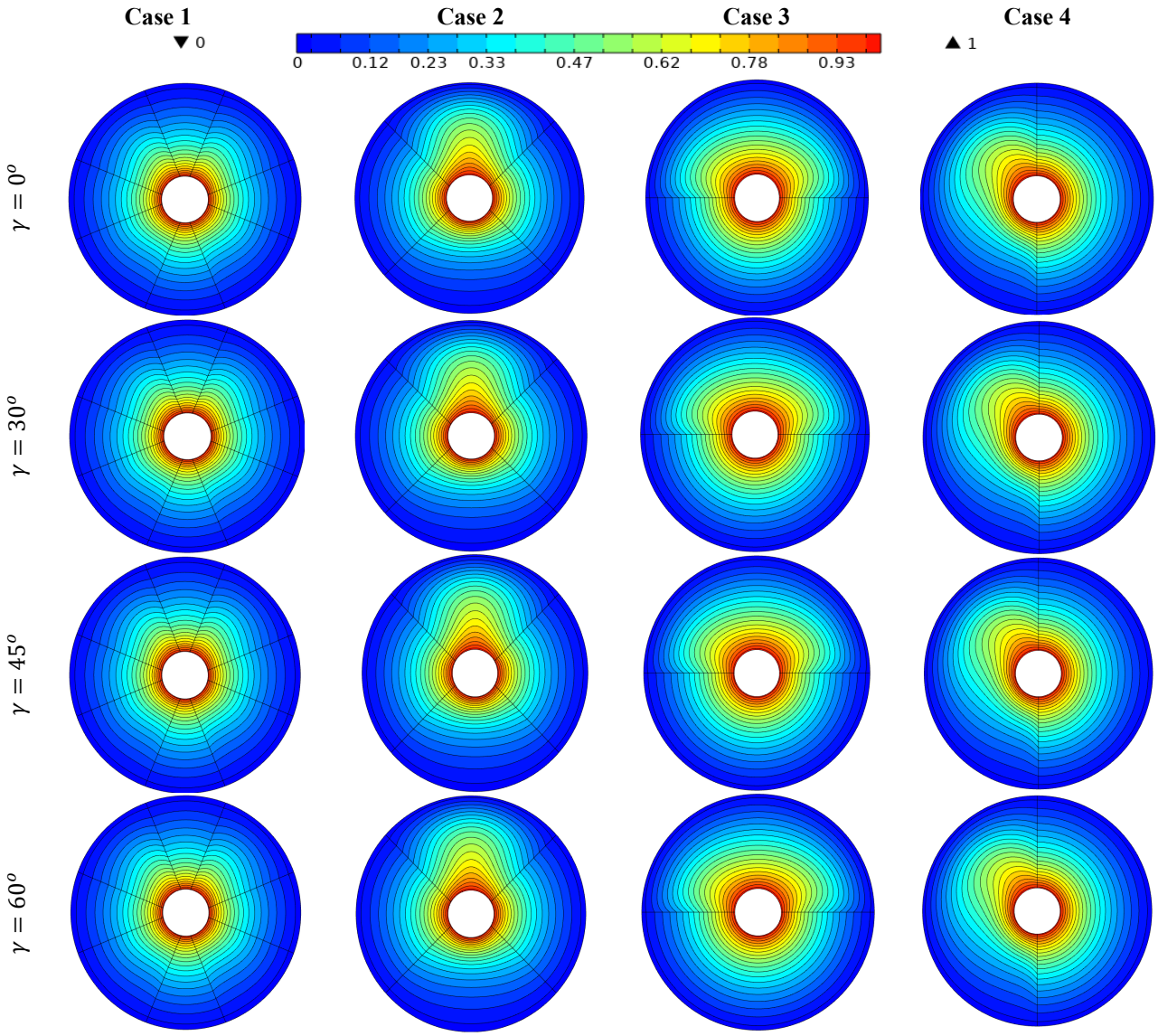

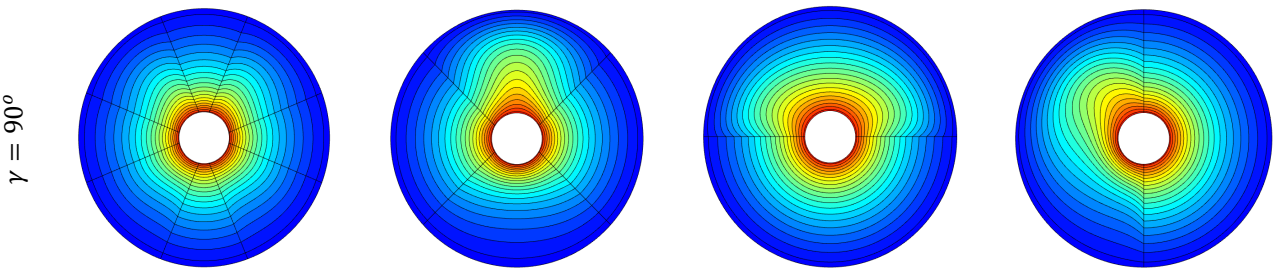

Figure 14. Isothermal contours at different values of magnetic field angle for different configurations at Ra = 10^5, Ha = 5, Da = 10^{-3}, φ = 0.01, λ = 1, Rd = 1

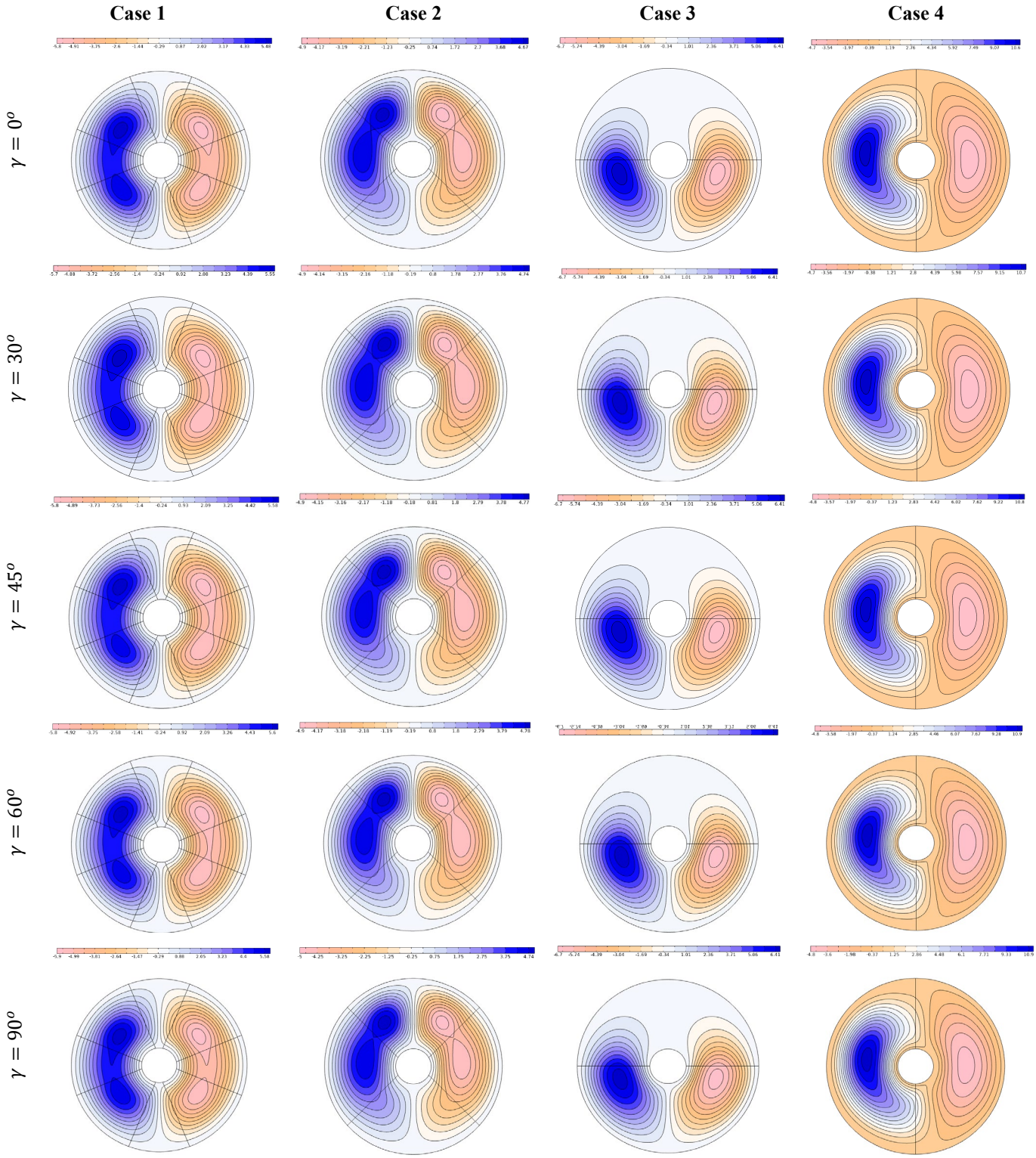

Figure 15. Stream function contours at different values of magnetic field angle for different configurations at Ra = 10^5, Ha = 5, Da = 10^{-3}, φ = 0.01, λ = 1, Rd = 1

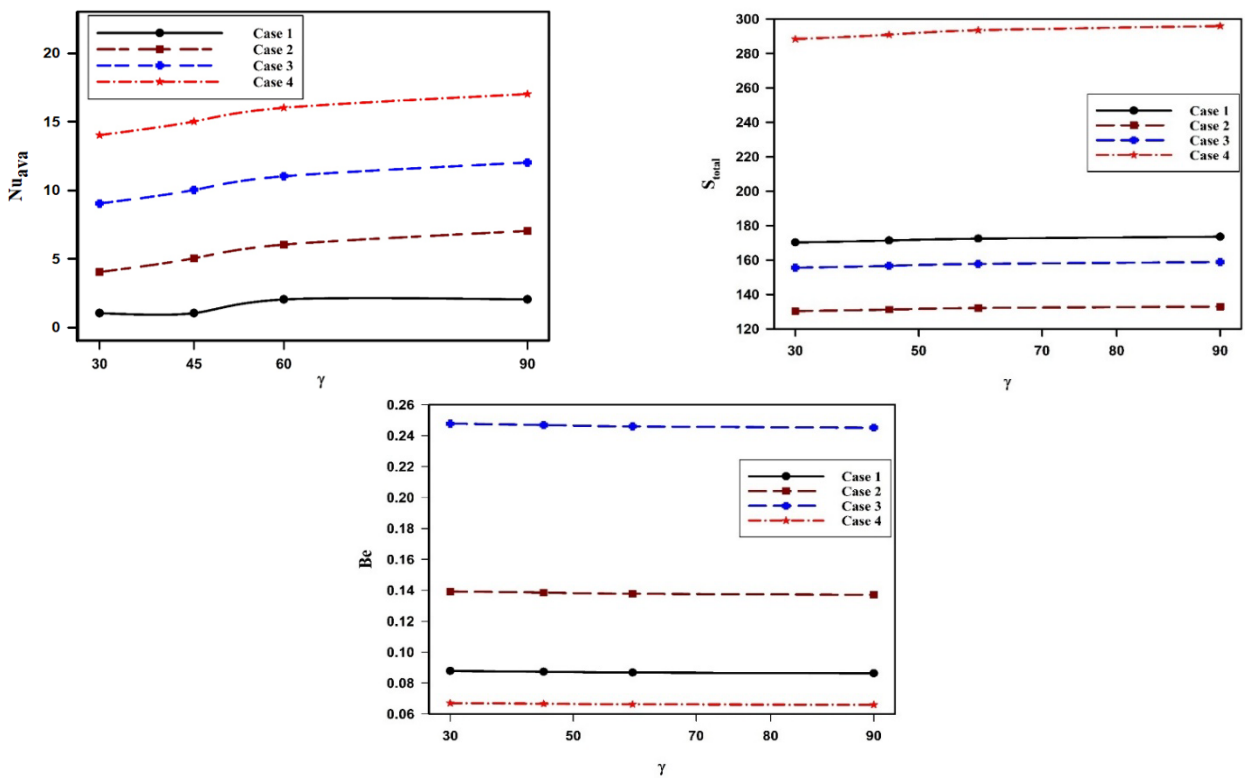

Figure 16. Effect of magnetic field angle for different cases on Nu_{av}, $S_{total,}$ and Be for Ra = 10^5, Da = 10^{-3}, φ = 0.01, λ = 1, Rd = 1

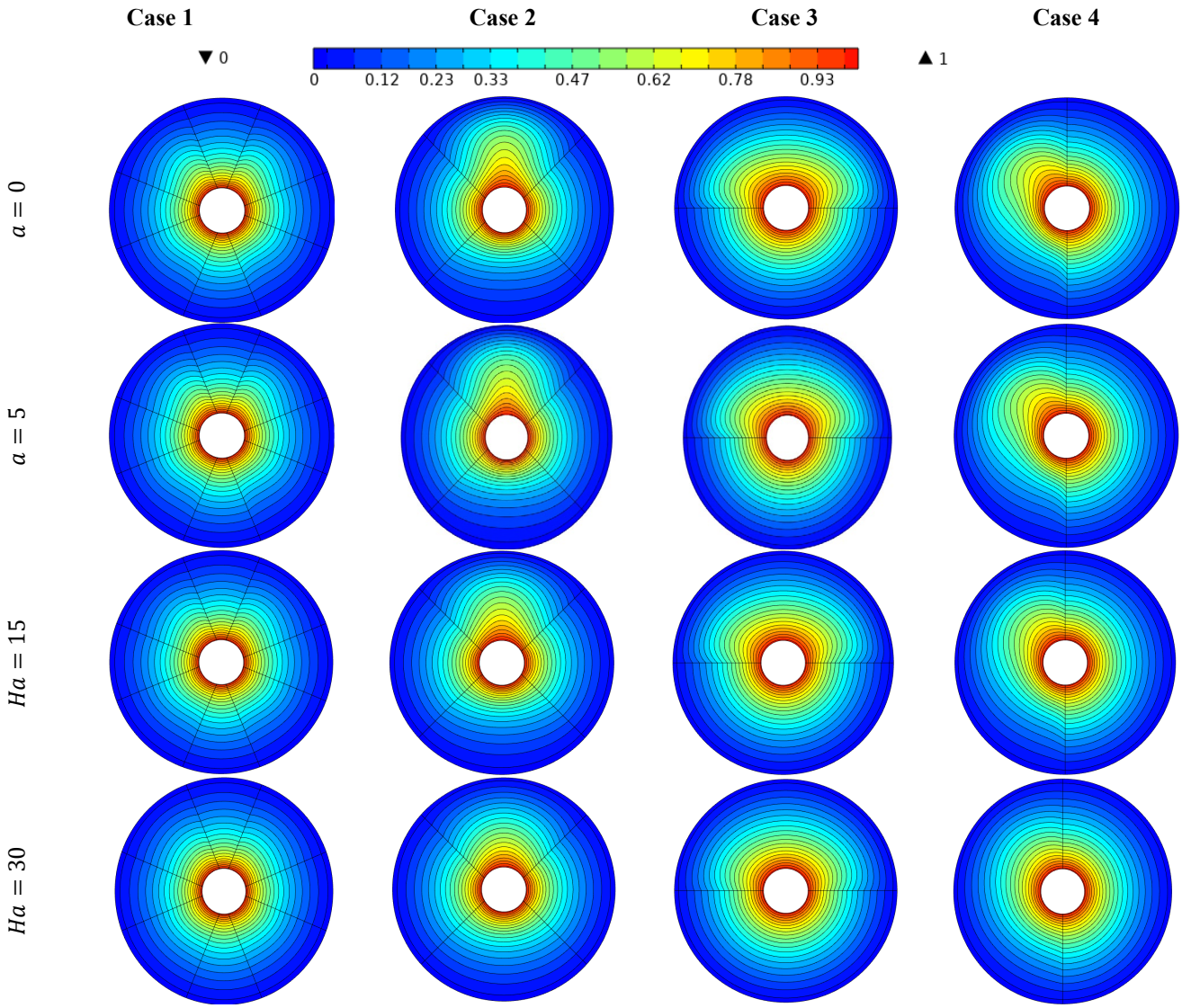

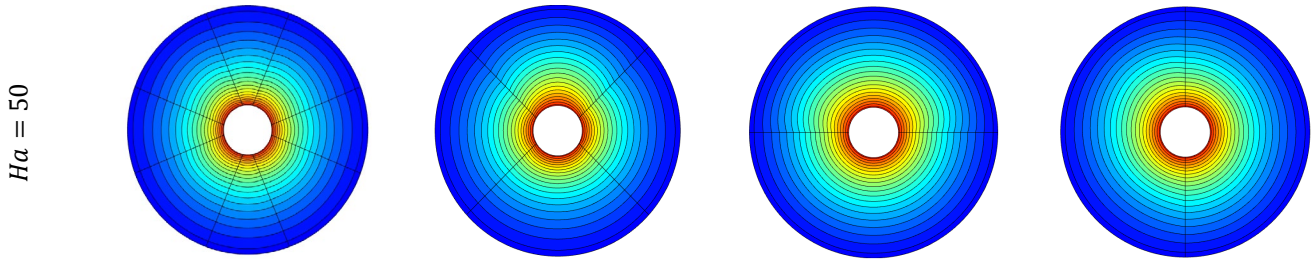

Figure 17. Isothermal contours at different values of Hartman number for different configurations at Ra = 10^5, γ = 0, Da = 10^{-3}, φ = 0.01, λ = 1, Rd = 1

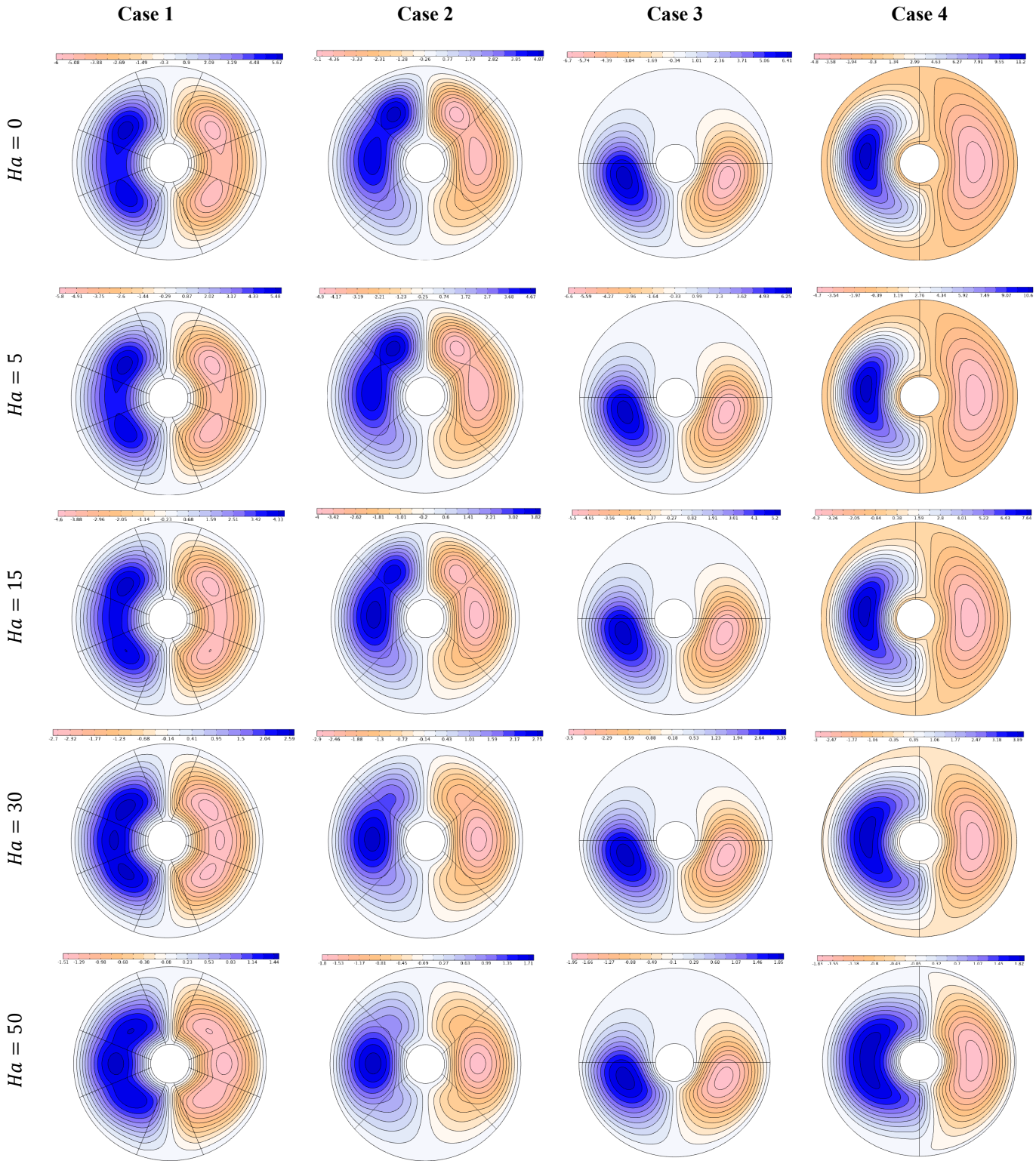

Figure 18. Stream function contours at different values of Hartman number for different configurations at Ra = 10^5, γ = 0, Da = 10^{-3}, φ = 0.01, λ = 1, Rd = 1

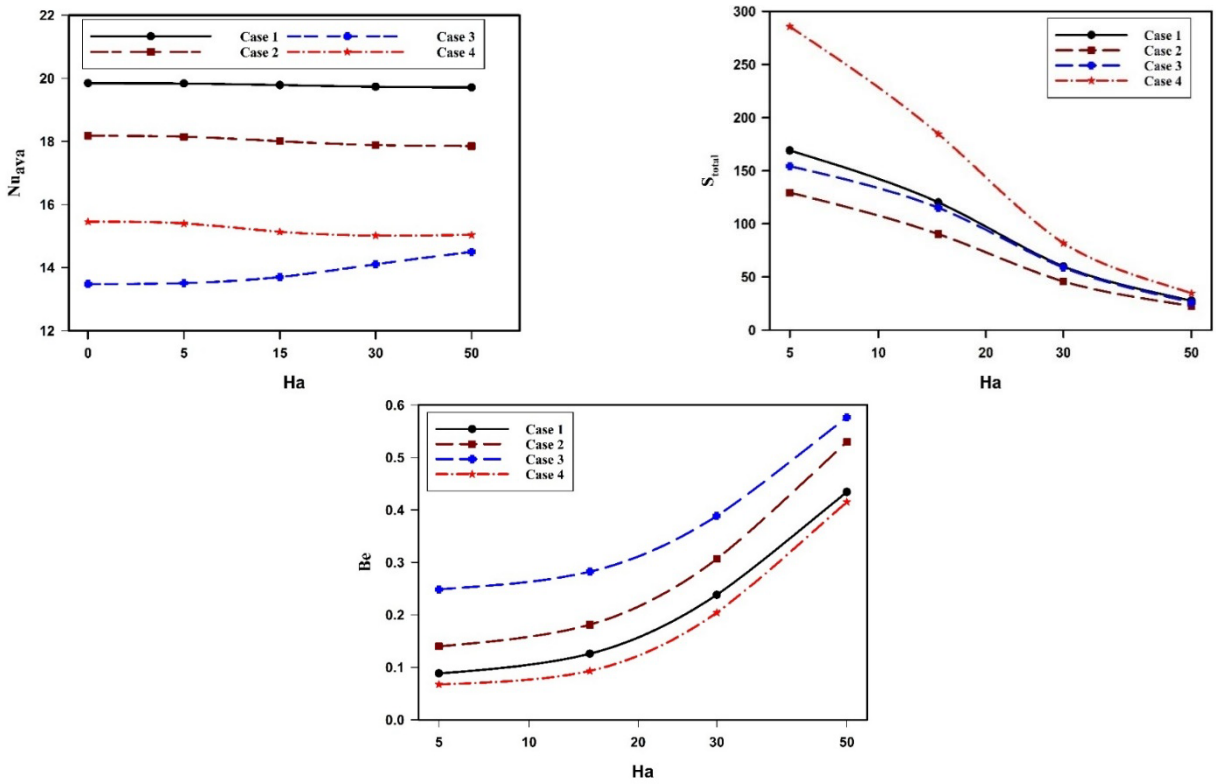

Figure 19. Effect of Hartman number for different cases on Nu_{av}, $S_{total,}$ and Be for Ra = 10^5, Da = 10^{-3}, γ = 0, φ = 0.01, λ = 1, Rd = 1

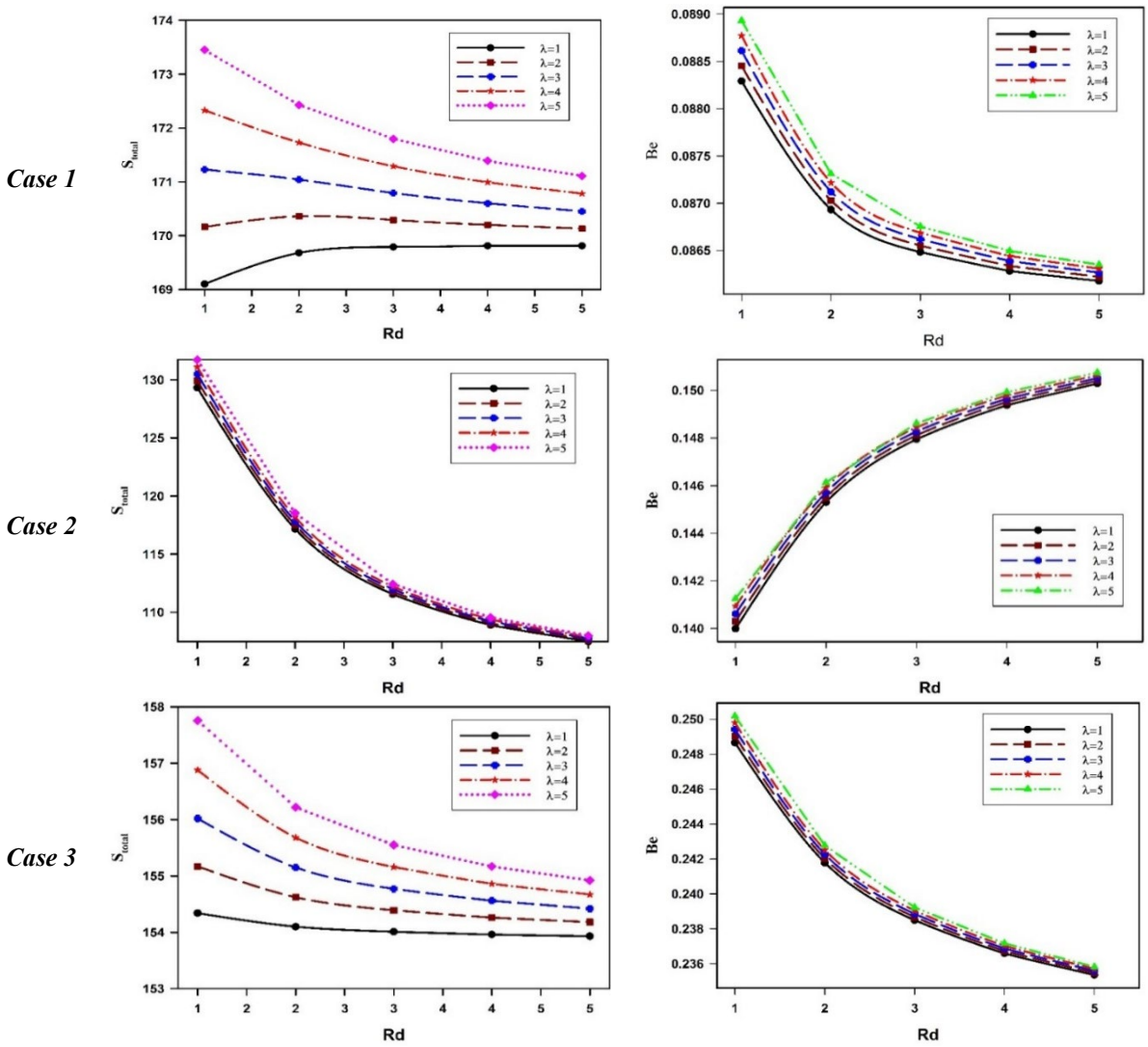

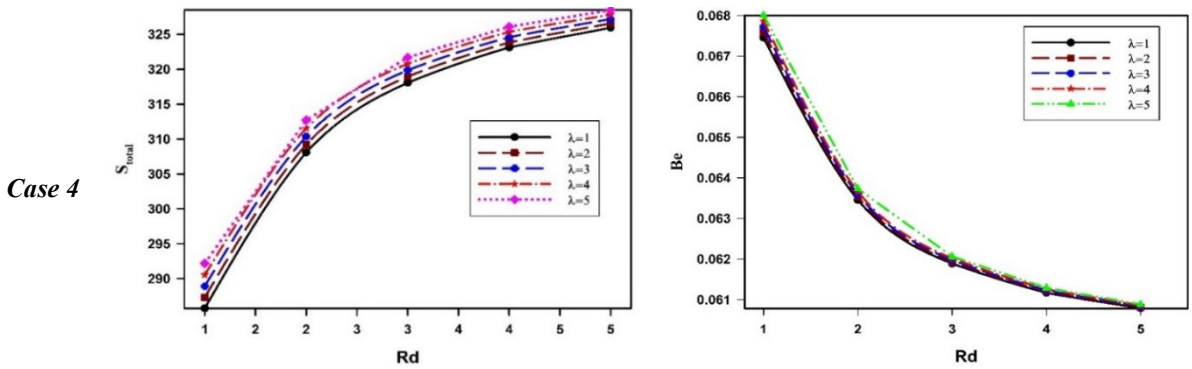

Figure 20. Effect of Rd and λ on S_{total} and Be for different cases at Ra = 10^5, γ = 0, Ha = 5, Da = 10^{-3}, φ = 0.01

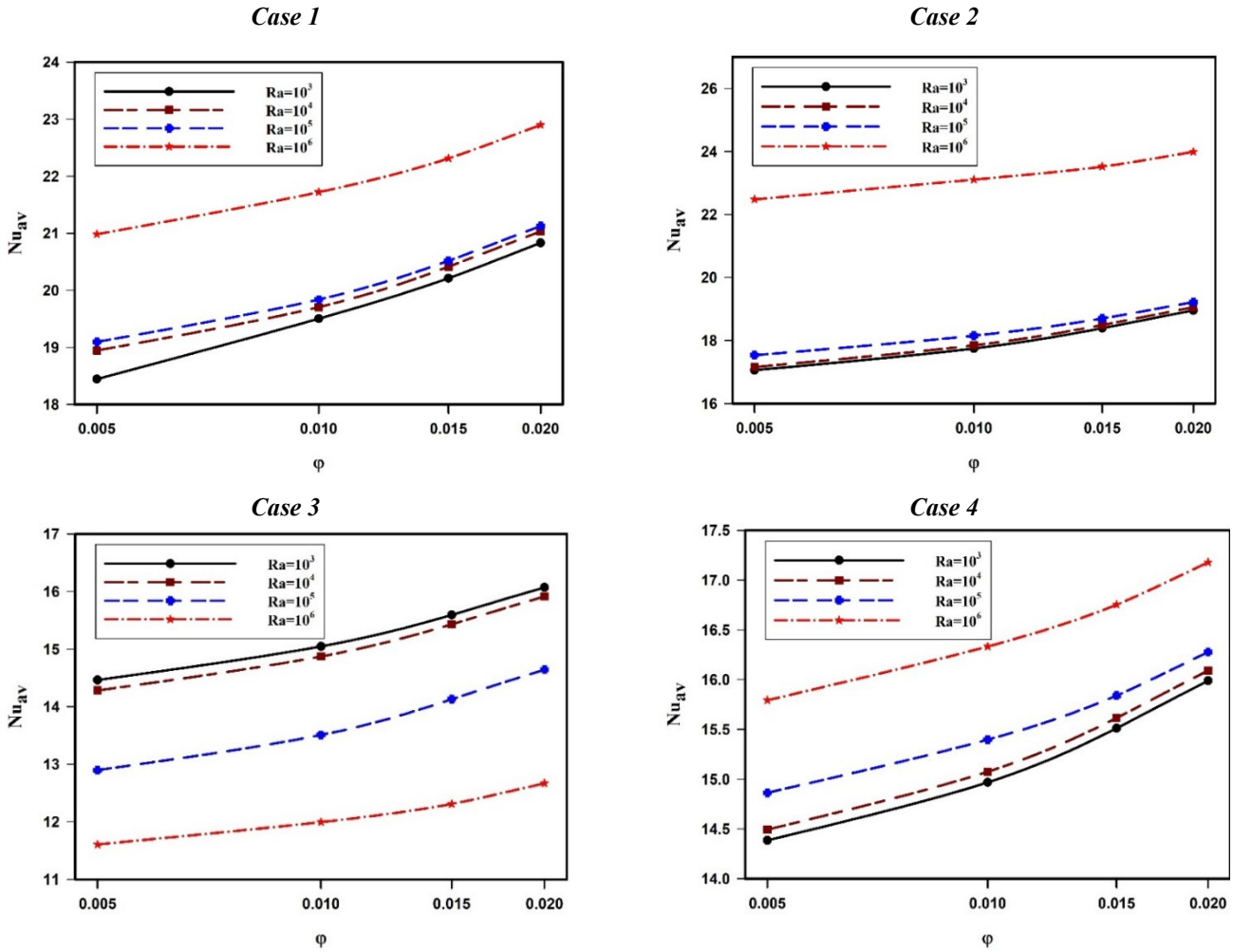

Figure 21. Effect of φ and Ra on Nu_{av} for different cases at λ = 1, Rd = 1, γ = 0, Ha = 5, Da = 10^{-3}

3.5 Effects of radiation and nanoparticle loading

Figure 20 illustrates the combined effects of radiation parameter (Rd) and heat-source parameter (λ) on total entropy generation (S_{total}) and Bejan number (Be) across the four porous layer configurations at fixed parameters (Ra = 10^5, γ = 0, Ha = 5, Da = 10^{-3}, φ = 0.01).

For Case 1 (symmetrical porous sections), S_{total} exhibits a non-monotonic response to increasing Rd values for any fixed λ. At λ = 1, S_{total} initially rises by 0.42% from Rd = 1 to Rd = 3 (169.1 to 169.79) before stabilizing at higher Rd values. As λ increases from 1 to 5 at fixed Rd = 1, S_{total} shows a consistent increase of 2.57% (169.1 to 173.45), indicating enhanced radiative entropy generation. However, this λ-sensitivity diminishes at higher Rd values, with only a 0.76% increase at Rd = 5 (169.81 to 171.11), suggesting a saturation effect in radiative heat transfer mechanisms.

Case 2 (diagonal porous arrangement) demonstrates markedly different behavior, with S_{total} decreasing significantly by 16.90% as Rd increases from 1 to 5 at λ = 1 (129.33 to 107.47). This indicates that enhanced radiation intensity reduces overall irreversibilities in this configuration, possibly by homogenizing temperature gradients. The influence of λ remains relatively modest, with only a 1.85% increase in S_{total} as λ rises from 1 to 5 at Rd = 1 (129.33 to 131.73).

For Case 3 (bottom-half porous layer), S_{total} shows remarkable stability across radiation parameters, decreasing

marginally by 0.27% as *Rd* increases from 1 to 5 at λ = 1 (154.34 to 153.93). The λ-dependency remains consistent, with approximately a 2.22% increase in S_{total} as λ rises from 1 to 5 at Rd = 1 (154.34 to 157.76). This stability suggests that the horizontal porous configuration maintains consistent entropy generation characteristics regardless of radiative parameters.

Case 4 (right-half porous configuration) displays the most pronounced response to radiation parameters, with S_{total} increasing significantly by 14.05% as Rd rises from 1 to 5 at λ = 1 (285.76 to 325.92). The λ-dependency remains modest, with an approximately 2.25% increase in S_{total} as λ increases from 1 to 5 at Rd = 1 (285.76 to 292.19). This substantial sensitivity to radiation intensity indicates that the vertical porous arrangement creates conditions where radiative heat transfer mechanisms significantly contribute to overall irreversibilities.

The Bejan number analysis reveals subtle yet consistent patterns across all configurations. For all cases, Be decreases with increasing Rd at any fixed λ, indicating that enhanced radiation intensity shifts the irreversibility balance toward fluid friction. This effect is most pronounced in Case 1, where Be decreases by 2.40% as Rd increases from 1 to 5 at λ = 1 (0.088291 to 0.086177). Conversely, the λ-dependency remains minimal across all cases, with Be increases of less than 1% as λ rises from 1 to 5 at any fixed Rd.

These complex responses to radiation parameters can be physically explained by the interaction between radiative heat transfer mechanisms and the specific flow structures induced by each porous configuration. Enhanced radiation intensity (higher Rd) tends to homogenize temperature gradients, which affects both thermal irreversibilities and flow patterns. In symmetric configurations (Case 1), this homogenization has a minimal impact on overall entropy generation, whereas in asymmetric arrangements (particularly Case 4), it significantly alters the landscape of irreversibility. The mean absorption coefficient (λ) consistently enhances radiative heat transfer, slightly increasing entropy generation across all configurations while maintaining the fundamental characteristics determined by the porous media distribution.

Figure 21 illustrates the combined effects of nanoparticle volume fraction (φ) and Rayleigh number (Ra) on the average Nusselt number (Nu_{av}), total entropy generation (S_{total}), and Bejan number (Be) for Cases 1 and 2 at fixed parameters (λ = 1, Rd = 1, γ = 0, Ha = 5, Da = 10^{-3}).

For Case 1 (symmetrical porous sections), Nu_{av} demonstrates a consistent positive correlation with nanoparticle concentration across all Rayleigh numbers. At Ra = 10^5, Nu_{av} increases by 10.64% as φ rises from 0.005 to 0.02 (19.096 to 21.128). This enhancement becomes more pronounced at higher Ra values, with a 9.12% increase at Ra = 10^6 (20.985 to 22.899). The augmentation of heat transfer performance with increasing nanoparticle concentration can be attributed to the enhanced thermal conductivity and specific heat capacity of the hybrid nanofluid, which improves conductive heat transfer mechanisms within the porous regions.

Case 2 (diagonal porous arrangement) exhibits similar trends, with Nu_{av} increasing by 13.55% as φ rises from 0.005 to 0.02 at Ra = 10^5 (12.896 to 14.643). However, the absolute Nu_{av} values are consistently lower than in Case 1, indicating that the diagonal porous arrangement provides less effective heat transfer pathways compared to the symmetrical configuration. Additionally, both cases show an increase in Nu_{av} with rising Ra for any fixed φ, demonstrating the fundamental enhancement of convective transport at higher buoyancy forces.

Regarding entropy generation, Case 1 shows a non-intuitive trend where S_{total} increases with φ at lower Ra values (Ra = 10^3 and 10^4) but decreases with φ at higher Ra values (Ra = 10^5 and 10^6). For instance, at Ra = 10^5, S_{total} decreases by 5.55% as φ increases from 0.005 to 0.02 (171.53 to 162.01). This behavior suggests that at high Ra values, the enhanced thermal homogenization provided by higher nanoparticle concentrations reduces thermal gradients and associated irreversibilities, despite the increased fluid friction from higher viscosity.

Conversely, Case 2 shows a more consistent pattern, with S_{total} generally increasing with φ across all Ra values, though the relationship becomes non-monotonic at Ra = 10^5 and 10^6. At Ra = 10^6, S_{total} increases by 1.72% as φ rises from 0.005 to 0.02 (14076 to 14318). This distinct entropy generation pattern highlights how the geometric arrangement of porous media fundamentally alters the thermodynamic response to nanoparticle addition.

The Bejan number analysis provides further insight into the dominant irreversibility mechanisms. For both cases, Be increases with φ at any fixed Ra, indicating that higher nanoparticle concentrations shift the irreversibility balance slightly toward thermal effects. This trend is consistent across all Ra values for Case 1, with Be increasing by 11.61% as φ rises from 0.005 to 0.02 at Ra = 10^5 (0.085344 to 0.095253). Similarly, Case 2 shows a modest 0.34% increase in Be under the same conditions (0.24781 to 0.24754).

Additionally, both cases exhibit a dramatic decrease in Be as Ra increases for any fixed φ, confirming the progressive dominance of fluid friction irreversibilities at higher convection regimes. This transition is particularly pronounced in Case 1, where Be plummets from 0.99388 at Ra = 10^3 to 0.0033988 at Ra = 10^6 for φ = 0.005, representing a 99.66% reduction.

3.6 Summary of key findings

The parametric study presented in Sections 3.2–3.5 reveals three overarching trends that directly answer the scientific questions posed in the Introduction. First, the spatial distribution of the porous layers — rather than the permeability level alone — emerges as the dominant geometric parameter controlling thermal performance: the diagonal arrangement (Case 2) outperforms all other configurations at high Rayleigh numbers, whereas the bottom-half arrangement (Case 3) consistently underperforms due to its obstruction of buoyancy-driven circulation. Second, the influence of the applied magnetic field is non-monotonic with respect to entropy generation: moderate Hartmann numbers (Ha ≈ 30) minimise the total irreversibilities by suppressing fluid-friction entropy, while stronger fields reintroduce electromagnetic-dissipation irreversibilities. By contrast, field orientation is shown to exert a negligible thermal effect (< 0.5% variation in Nu_{av}). Third, the benefit of Ag–MgO hybrid nanoparticle loading is strongly configuration-dependent: it enhances heat transfer most effectively in symmetrical arrangements (Cases 1 and 2), while radiation parameters display the strongest sensitivity in the asymmetric Case 4. These findings collectively indicate that, for the annular geometry considered, geometric optimisation of the porous-layer distribution should be the primary design lever, with

magnetic-field strength and nanoparticle loading serving as secondary fine-tuning mechanisms.

4. CONCLUSIONS

This study presented a numerical investigation of MHD natural convection of an Ag–MgO/water hybrid nanofluid in an annular double-pipe heat exchanger containing four distinct porous-layer configurations, with combined radiation and electromagnetic effects. The principal conclusions drawn from the parametric analysis are summarised below:

1. The spatial distribution of the porous layers was identified as the dominant geometric parameter governing thermal performance, with the diagonal arrangement (Case 2) providing the highest heat-transfer enhancement and the bottom-half arrangement (Case 3) exhibiting the weakest performance under dominant convection conditions.
2. The influence of the magnetic field on entropy generation was found to be strongly non-monotonic: moderate Hartmann numbers minimise total irreversibilities by suppressing fluid-friction entropy, whereas stronger fields reintroduce electromagnetic-dissipation losses.
3. Hybrid nanoparticle loading consistently improved heat transfer in symmetrical porous configurations while simultaneously reducing entropy generation, demonstrating a favourable coupling between thermal enhancement and thermodynamic efficiency.
4. The orientation of the magnetic field was shown to exert a negligible influence on the overall thermal performance, indicating that, for the geometry considered, design optimisation should prioritise the porous-layer distribution and field magnitude rather than its direction.
5. Radiation effects were found to be strongly configuration-dependent, emphasising the need to select the porous-layer arrangement in accordance with the expected radiative operating conditions of the target application.

From a practical design perspective, the present findings translate into the following guidelines: for applications prioritising maximum heat transfer (e.g., concentrated solar-thermal receivers operating at $Ra \geq 10^5$), a diagonal porous-sector arrangement (Case 2) combined with a hybrid nanoparticle loading of $\varphi = 0.02$ is recommended. For applications where thermodynamic efficiency is critical such as liquid-metal cooling loops in compact nuclear and fusion reactors-operating under strong magnetic confinement a symmetrical arrangement (Case 1) with a moderate Hartmann number ($Ha \approx 30$) minimises total entropy generation by up to 73%. For power-electronics thermal management and MHD-assisted cooling systems, a balanced operation at $Ra = 10^5$, $Ha = 15–30$, and $\varphi = 0.01$ offers a favourable compromise between enhanced heat transfer and reduced irreversibilities. These recommendations provide direct guidance for engineers designing annular heat exchangers where porous media, hybrid nanofluids, and electromagnetic effects interact.

It is important to acknowledge several limitations of the present investigation, which also define promising directions for future research. First, the analysis has been conducted under a two-dimensional, laminar, and steady-state framework; although this is sufficient to capture the dominant physical mechanisms, extension to three-dimensional and transient simulations would provide a more complete picture, particularly at the highest Rayleigh numbers considered where flow instabilities may emerge. Second, the hybrid nanofluid has been treated as a single-phase, Newtonian, and incompressible medium using the Boussinesq approximation, neglecting Brownian motion, thermophoresis, and nanoparticle sedimentation effects; a two-phase or Buongiorno-type model could further refine the predictions at high volume fractions. Third, the Rosseland approximation adopted for radiative heat transfer is strictly valid for optically thick media; alternative radiation models (e.g., P1 or discrete ordinates) may be required for optically thin regimes. Fourth, the porous medium has been assumed isotropic, homogeneous, and in local thermal equilibrium with the fluid, whereas anisotropic or thermally non-equilibrium formulations could reveal additional design degrees of freedom. Finally, experimental validation using prototype annular heat exchangers remains a valuable future task to complement the present numerical findings. Addressing these aspects constitutes the natural continuation of this research.

ACKNOWLEDGMENT

The researchers acknowledge the support provided by the Department of Mechanical Engineering, University of Al-Qadisiyah, Iraq.

REFERENCES

[1] Luo, J., Shao, Y., Yan, Z., Han, X., Guo, Q. (2025). Thermal performance enhancement of borehole heat exchangers by thermally induced groundwater convection in aquifers. Renewable Energy, 243: 122539. https://doi.org/10.1016/j.renene.2025.122539

[2] Rahimi, A., Saee, A.D., Kasaeipoor, A., Hooshmand, P., Malekshah, E.H. (2018). Lattice boltzmann simulation for hydrothermal analysis of free convection within dumbbell-shaped heat exchanger. Chinese Journal of Physics, 56(6): 2865-2878. https://doi.org/10.1016/j.cjph.2018.09.022

[3] Hassan, A.M., Alwan, A.A., Hamzah, H.K. (2023). Numerical study of fan coil heat exchanger with copper-foam. International Journal of Fluid Machinery and Systems, 16(1): 73-88. https://doi.org/10.5293/IJFMS.202316.1.073

[4] Nasrin, R., Parvin, S., Alim, M.A. (2013). Effect of Prandtl number on free convection in a solar collector filled with nanofluid. Procedia Engineering, 56: 54-62. https://doi.org/10.1016/j.proeng.2013.03.088

[5] Prakash, R., Gnanasekaran, A., Rengasamy, M., Rajaram, K. (2025). A review on recent developments in natural convective solar dryer for agricultural products: Methods, collector design, influencing factors, performance and challenges. Renewable and Sustainable Energy Reviews, 215: 115613. https://doi.org/10.1016/j.rser.2025.115613

[6] Talha, T., Talha, M., Liu, S., Mazhar, A.R., Perwez, U., Moiz, M., Afzal, A. (2025). Experimental study of unglazed transpired solar collectors integrated with buildings in humid sub-tropics. Energy and Buildings, 339: 115767.

https://doi.org/10.1016/j.enbuild.2025.115767
[7] Hassan, A.M., Alomari, M.A., Ahmed, L.M., Kh, T.I., Alqurashi, F., Jabbar, O. (2026). Turbulent forced convection and entropy generation analysis in a rectangular channel with t-shaped rib turbulators and CuO/water nanofluid. Results in Engineering, 30: 110364. https://doi.org/10.1016/j.rineng.2026.110364
[8] Mehta, S.K., Kumar, D., Mondal, P.K., Wongwises, S. (2024). Characterisation of conjugate forced convection in a wavy solar power plant: The role of porous metallic blocks. Chemical Engineering and Processing-Process Intensification, 196: 109615. https://doi.org/10.1016/j.cep.2023.109615
[9] Sadeghi, M.S., Dogonchi, A.S., Ghodrat, M., Chamkha, A.J., Alhumade, H., Karimi, N. (2021). Natural convection of CuO-water nanofluid in a conventional oil/water separator cavity: Application to combined-cycle power plants. Journal of the Taiwan Institute of Chemical Engineers, 124: 307-319. https://doi.org/10.1016/j.jtice.2021.03.031
[10] Tagle-Salazar, P.D., Cabeza, L.F., Prieto, C. (2024). Transient performance modelling of solar tower power plants with molten salt thermal energy storage systems. Journal of Energy Storage, 97: 112793. https://doi.org/10.1016/j.est.2024.112793
[11] Alshammari, M., Alalou, A., Aldawood, S., Qi, B., Al-Dahhan, M.H. (2024). Investigation of convective heat transfer in a cold flow pebble bed nuclear reactor using advanced pebble probe heat transfer sensor. Experimental Thermal and Fluid Science, 154: 111148. https://doi.org/10.1016/j.expthermflusci.2024.111148
[12] Freile, R., Tano, M.E., Ragusa, J.C. (2023). Lattice Boltzmann solidification modeling of forced convection internal flows applied to Gen-IV nuclear reactor coolants. Progress in Nuclear Energy, 163: 104785. https://doi.org/10.1016/j.pnucene.2023.104785
[13] Hamtiaux, V., Ruyer, P., Bartosiewicz, Y. (2025). Natural convection through and over a heating porous medium: Towards high fidelity simulations of nuclear spent fuel pools. International Journal of Heat and Fluid Flow, 112: 109724. https://doi.org/10.1016/j.ijheatfluidflow.2024.109724
[14] Ullah, Z., Alam, M.M., El-Zahar, E.R., Shahab, S., Abu-Zinadah, H., Ebaid, A., Alsulami, M.D., Seddek, L.F. (2025). Williamson nanofluid aspects on fluctuating radiative heat and mass transfer with viscous dissipation along heat exchanger plate in nuclear-power plants. Case Studies in Thermal Engineering, 71: 106176. https://doi.org/10.1016/j.csite.2025.106176
[15] Al-Weheibi, S.M., Rahman, M.M., Saghir, M.Z. (2023). Three-dimensional non-Darcy free convective heat transfer flow in a bidisperse porous medium within a cubical cavity. International Journal of Thermofluids, 20: 100413. https://doi.org/10.1016/j.ijft.2023.100413
[16] Sannagoudra, A., Sharma, G., Varma, S.V.K., Ibrahim, A.A., El-Meligy, M.A., Tawade, J.V., Ameen, H.F.M., Batool, N. (2025). Electromagnetic free convective flow of a radiative, chemically reactive hybrid nanofluid over a moving vertical surface: With effects of porous medium. Journal of Radiation Research and Applied Sciences, 18(2): 101365. https://doi.org/10.1016/j.jrras.2025.101365
[17] Yan, G., Shawabkeh, A., Chaturvedi, R., Nur-Firyal, R., Youshanlouei, M.M. (2022). Using MHD free convection to receive the generated heat by an elliptical porous media. Case Studies in Thermal Engineering, 36: 102153. https://doi.org/10.1016/j.csite.2022.102153
[18] Sarma, S., Ahmed, N. (2022). Thermal diffusion effect on unsteady MHD free convective flow past a semi-infinite exponentially accelerated vertical plate in a porous medium. Canadian Journal of Physics, 100(10): 437-451. https://doi.org/10.1139/cjp-2021-0361
[19] Nayar, H., Phiri, P.A. (2025). Investigation of heat and mass transfer of free convective MHD flow along a vertical plate in a porous medium using the new modified differential transform-decomposition method. Results in Engineering, 25: 104083. https://doi.org/10.1016/j.rineng.2025.104083
[20] Goud, B.S., Srilatha, P., Srinivasulu, T., Reddy, Y.D., Kumar, K.S. (2023). Induced by heat source on unsteady MHD free convective flow of Casson fluid past a vertically oscillating plate through porous medium utilizing finite difference method. Materials Today: Proceedings. https://doi.org/10.1016/j.matpr.2023.01.378
[21] Groşan, T., Revnic, C., Pop, I., Ingham, D.B. (2015). Free convection heat transfer in a square cavity filled with a porous medium saturated by a nanofluid. International Journal of Heat and Mass Transfer, 87: 36-41. https://doi.org/10.1016/j.ijheatmasstransfer.2015.03.078
[22] Baytaş, A.C., Pop, I. (2001). Natural convection in a trapezoidal enclosure filled with a porous medium. International Journal of Engineering Science, 39(2): 125-134. https://doi.org/10.1016/S0020-7225(00)00033-1
[23] Beckermann, C., Viskanta, R., Ramadhyani, S. (1986). A numerical study of non-Darcian natural convection in a vertical enclosure filled with a porous medium. Numerical Heat Transfer, 10(6): 557-570. https://doi.org/10.1080/10407788608913535
[24] Batool, S., Nawaz, M. (2020). Investigation of thermal enhancement in non-Newtonian fluid with hybrid micro-structures in an enclosure. International Communications in Heat and Mass Transfer, 117: 104777. https://doi.org/10.1016/j.icheatmasstransfer.2020.104777
[25] Rehman, K.U., Malik, M.Y., Al-Mdallal, Q.M., Al-Kouz, W. (2020). Heat transfer analysis on buoyantly convective non-Newtonian stream in a hexagonal enclosure rooted with T-Shaped flipper: Hybrid meshed analysis. Case Studies in Thermal Engineering, 21: 100725. https://doi.org/10.1016/j.csite.2020.100725
[26] Hameed, R.H., Hussein, R.A., Al-Salami, Q.H., Alomari, M.A., Hassan, A.M., Alyousuf, F.Q., Alqurashi, F., Flayyih, M.A. (2025). Free convection investigation for a Casson-based Cu− H_2O nanofluid in semi parabolic enclosure with corrugated cylinder. Heliyon, 11(1): e40960. https://doi.org/10.1016/j.heliyon.2024.e40960
[27] Hassan, A.M., Alomari, M.A., Birdawod, H.Q., Alyousuf, F.Q., Alqurashi, F., Flayyih, M.A., Sadeq, A.M. (2025). Hydrothermal and entropy analysis of micro-polar NEPCM with exothermic reactions and magnetic fields. Energy, 316: 134479. https://doi.org/10.1016/j.energy.2025.134479
[28] Bourantas, G.C., Skouras, E.D., Loukopoulos, V.C., Burganos, V.N. (2014). Heat transfer and natural convection of nanofluids in porous media. European Journal of Mechanics-B/Fluids, 43: 45-56.

https://doi.org/10.1016/j.euromechflu.2013.06.013
[29] Fattahi, E., Farhadi, M., Sedighi, K., Nemati, H. (2012). Lattice Boltzmann simulation of natural convection heat transfer in nanofluids. International Journal of Thermal Sciences, 52: 137-144. https://doi.org/10.1016/j.ijthermalsci.2011.09.001
[30] Haddad, Z., Oztop, H.F., Abu-Nada, E., Mataoui, A. (2012). A review on natural convective heat transfer of nanofluids. Renewable and Sustainable Energy Reviews, 16(7): 5363-5378. https://doi.org/10.1016/j.rser.2012.04.003
[31] Lin, K.C., Violi, A. (2010). Natural convection heat transfer of nanofluids in a vertical cavity: Effects of non-uniform particle diameter and temperature on thermal conductivity. International Journal of Heat and Fluid Flow, 31(2): 236-245. https://doi.org/10.1016/j.ijheatfluidflow.2009.11.003
[32] Oueslati, F.S., Bennacer, R. (2011). Heterogeneous nanofluids: natural convection heat transfer enhancement. Nanoscale Research Letters, 6(1): 222. https://doi.org/10.1186/1556-276X-6-222
[33] Pakravan, H.A., Yaghoubi, M. (2013). Analysis of nanoparticles migration on natural convective heat transfer of nanofluids. International Journal of Thermal Sciences, 68: 79-93. https://doi.org/10.1016/j.ijthermalsci.2012.12.012
[34] Sabri, L.S., Ali, A.B.M., Akbari, O.A., Montazerifar, F., Kahbandeh, F., Salahshour, S., Mokhtarian, A. (2025). Natural convection of water/Titanium oxide nanofluid inside a closed enclosure at different angles of attack. International Journal of Thermofluids, 27: 101161. https://doi.org/10.1016/j.ijft.2025.101161
[35] Rashad, A.M., Rashidi, M.M., Lorenzini, G., Ahmed, S.E., Aly, A.M. (2017). Magnetic field and internal heat generation effects on the free convection in a rectangular cavity filled with a porous medium saturated with Cu–water nanofluid. International Journal of Heat and Mass Transfer, 104: 878-889. https://doi.org/10.1016/j.ijheatmasstransfer.2016.08.025
[36] Nayak, M.K., Dogonchi, A.S., Rahbari, A. (2023). Free convection of Al_2O_3-water nanofluid inside a hexagonal-shaped enclosure with cold diamond-shaped obstacles and periodic magnetic field. Case Studies in Thermal Engineering, 50: 103429. https://doi.org/10.1016/j.csite.2023.103429
[37] Mehryan, S.A., Kashkooli, F.M., Ghalambaz, M., Chamkha, A.J. (2017). Free convection of hybrid Al_2O_3-Cu water nanofluid in a differentially heated porous cavity. Advanced Powder Technology, 28(9): 2295-2305. https://doi.org/10.1016/j.apt.2017.06.011
[38] Turabi, Y.U.U.B., Munir, S., Nawaz, R. (2025). Entropy generation and magnetohydrodynamic influences on hybrid nanofluid convection in a staggered cavity. International Journal of Thermofluids, 27: 101204. https://doi.org/10.1016/j.ijft.2025.101204
[39] Khatun, S., Kundu, R., Islam, S., Aktary, R., Kumar, D. (2025). Sensitivity analysis on natural convective trapezoidal cavity containing hybrid nanofluid with magnetic effect: Numerical and statistical approach. Heliyon, 11(1): e41508. https://doi.org/10.1016/j.heliyon.2024.e41508
[40] Aissa, A., Belazreg, A., Laidoudi, H., Mohammed, S., Younis, O., Alazzam, A. (2024). Enhanced heat transmission in a triangular enclosure with a rotating cooled wall using nano-encapsulated phase change material nanofluid under mixed convection. Case Studies in Thermal Engineering, 54: 103992. https://doi.org/10.1016/j.csite.2024.103992
[41] Aboud, E.D., Rashid, H.K., Jassim, H.M., Ahmed, S.Y., Khafaji, S.O.W., Hamzah, H.K., Ali, F.H. (2020). MHD effect on mixed convection of annulus circular enclosure filled with non-newtonian nanofluid. Heliyon, 6(4): e03773. https://doi.org/10.1016/j.heliyon.2020.e03773
[42] Kefayati, G.H.R. (2017). Simulation of natural convection and entropy generation of non-Newtonian nanofluid in a porous cavity using Buongiorno's mathematical model. International Journal of Heat and Mass Transfer, 112: 709-744. https://doi.org/10.1016/j.ijheatmasstransfer.2017.04.121
[43] Masuda, T., Tagawa, T. (2020). Axisymmetric natural convection of liquid metal in an annular enclosure under the influence of azimuthal magnetic field. Energies, 13(11): 2896. https://doi.org/10.3390/en13112896
[44] Raju, C.S.K., Sandeep, N. (2016). Heat and mass transfer in MHD non-Newtonian bio-convection flow over a rotating cone/plate with cross diffusion. Journal of Molecular Liquids, 215: 115-126. https://doi.org/10.1016/j.molliq.2015.12.058
[45] Alomari, M.A., Hassan, A.M., Alajmi, A., Salho, A.K., Sadeq, A.M., Alqurashi, F., Flayyih, M.A. (2025). Analysis of double-diffusive transport and entropy generation in a wavy cylindrical enclosure with inner heated core: Effects of MHD and radiation on casson Cu-H_2O nanofluid. Energy Science & Engineering, 13(6): 2810-2841. https://doi.org/10.1002/ese3.70069
[46] Hassan, A.M., Alomari, M.A., Sadeq, A.M., Alqurashi, F., Flayyih, M.A. (2025). Double diffusive mixed convection and entropy generation analysis of NEPCM-water mixture in a π-shaped cavity. International Communications in Heat and Mass Transfer, 167: 109395. https://doi.org/10.1016/j.icheatmasstransfer.2025.109395
[47] Kefayati, G.R. (2014). Simulation of magnetic field effect on natural convection of non-Newtonian power-law fluids in a sinusoidal heated cavity using FDLBM. International Communications in Heat and Mass Transfer, 53: 139-153. https://doi.org/10.1016/j.icheatmasstransfer.2014.02.026
[48] Devi, T.S., Lakshmi, C.V., Venkatadri, K., Reddy, M.S. (2021). Influence of external magnetic wire on natural convection of non-Newtonian fluid in a square cavity. Partial Differential Equations in Applied Mathematics, 4: 100041. https://doi.org/10.1016/j.padiff.2021.100041
[49] Hassan, A.M., Alomari, M.A., Al-Salami, Q.H., Alyousuf, F.Q., Alqurashi, F., Flayyih, M.A. (2024). Numerical analysis of free convection under the influence of radiation and inclined MHD in a triangular cavity filled with hybrid nanofluid and a porous fin. International Journal of Thermofluids, 24: 100843. https://doi.org/10.1016/j.ijft.2024.100843
[50] Alomari, M.A., Al-Farhany, K., Al-Salami, Q.H., Al-Jaburi, K., Alyousuf, F.Q., Ali, I.R., Biswas, N. (2023). Magnetohydrodynamic mixed convection in lid-driven curvilinear enclosure with nanofluid and partial porous layer. Journal of Magnetism and Magnetic Materials, 582: 170952.

https://doi.org/10.1016/j.jmmm.2023.170952
[51] Mondal, P., Mahapatra, T.R. (2021). MHD double-diffusive mixed convection and entropy generation of nanofluid in a trapezoidal cavity. International Journal of Mechanical Sciences, 208: 106665. https://doi.org/10.1016/j.ijmecsci.2021.106665
[52] Hassan, A.M., Alomari, M.A., Ghalambaz, M., Jabbar, O., Alqurashi, F., Flayyih, M.A. (2026). Numerical analysis of magnetohydrodynamic mixed convection for electronic thermal management: Coupling nano-encapsulated PCM with double-diffusive transport. Results in Engineering, 29: 109380. https://doi.org/10.1016/j.rineng.2026.109380
[53] Salho, A.K., Hassan, A.M., Alajmi, A., Alomari, M.A., Sadeq, A.M., Alqurashi, F., Flayyih, M.A. (2025). Thermo-fluid dynamics of Cu-H_2O Casson fluid in an H-shaped enclosure with corrugated cylinders: A study of entropy generation, MHD, and radiation effects. Results in Engineering, 25: 104346. https://doi.org/10.1016/j.rineng.2025.104346
[54] Uddin, M.J., Bég, O.A., Ismail, A.I. (2015). Radiative convective nanofluid flow past a stretching/shrinking sheet with slip effects. Journal of Thermophysics and Heat Transfer, 29(3): 513-523. https://doi.org/10.2514/1.T4372
[55] Bejan, A., Kestin, J. (1983). Entropy generation through heat and fluid flow. Journal of Applied Mechanics, 50(2): 475. https://doi.org/10.1115/1.3167071
[56] Alomari, M.A., Hassan, A.M., Sadeq, A.M., Alqurashi, F., Jabbar, O., Flayyih, M.A. (2026). Thermodynamic analysis of a multi-port NEPCM cooling device: Effects of mixed convection and magnetohydrodynamics on heat dissipation. International Communications in Heat and Mass Transfer, 172: 110736. https://doi.org/10.1016/j.icheatmasstransfer.2026.110736
[57] Hameed, R.H., Hassan, A.M., Hussein, R.A., Oliwie, A., Hamza, N.H. (2024). CFD analysis of mixed convection and entropy generation in vented curved cavity under the radiation effects. The European Physical Journal Plus, 139(8): 756. https://doi.org/10.1140/epjp/s13360-024-05546-9
[58] Esfe, M.H., Arani, A.A.A., Rezaie, M., Yan, W.M., Karimipour, A. (2015). Experimental determination of thermal conductivity and dynamic viscosity of Ag–MgO/water hybrid nanofluid. International Communications in Heat and Mass Transfer, 66: 189-195. https://doi.org/10.1016/j.icheatmasstransfer.2015.06.003
[59] Alomari, M.A., Al-Farhany, A., Hashem, A.L., Al-Dawody, M.F., Redouane, F., Olayemi, O.A. (2021). Numerical study of MHD natural convection in trapezoidal enclosure filled with (50%MgO-50%Ag/water) hybrid nanofluid: heated sinusoidal from below. International Journal of Heat and Technology, 39(4): 1271-1279. https://doi.org/10.18280/ijht.390425
[60] Ghalambaz, M., Doostani, A., Izadpanahi, E., Chamkha, A.J. (2020). Conjugate natural convection flow of Ag–MgO/water hybrid nanofluid in a square cavity. Journal of Thermal Analysis & Calorimetry, 139(3): 2321-2336. https://doi.org/10.1007/s10973-019-08617-7
[61] Chen, C.L., Cheng, C.H. (2004). Experimental and numerical study of mixed convection and flow pattern in a lid-driven arc-shape cavity. Heat and Mass Transfer, 41(1): 58-66. https://doi.org/10.1007/s00231-004-0541-5
[62] Alhashash, A., Saleh, H. (2023). Conjugate free convection from an array of discrete heat sources with water and nano-encapsulated phase change particle in a cold enclosure. Journal of Energy Storage, 57: 106076. https://doi.org/10.1016/j.est.2022.106076
[63] Kuehn, T.H., Goldstein, R.J. (1976). An experimental and theoretical study of natural convection in the annulus between horizontal concentric cylinders. Journal of Fluid Mechanics, 74(4): 695-719. https://doi.org/10.1017/S0022112076002012
[64] Basak, T., Roy, S., Paul, T., Pop, I. (2006). Natural convection in a square cavity filled with a porous medium: Effects of various thermal boundary conditions. International Journal of Heat and Mass Transfer, 49(7-8): 1430-1441. https://doi.org/10.1016/j.ijheatmasstransfer.2005.09.018

NOMENCLATURE

Be	Bejan number
B_0	magnetic field strength, T
D	outer diameter of annular channel, m
Da	Darcy number
g	Gravitational acceleration, m/s²
Ha	Hartmann number
k	thermal conductivity, W/m·K
Nu	Nusselt number
Nu_{av}	average Nusselt number
p	pressure, Pa
Pr	Prandtl number
Ra	Rayleigh number
Rd	Radiation parameter
Re	Reynolds number
S_{total}	total entropy generation, W/K
T	temperature, K
Th	hot wall temperature, K
Tc	cold wall temperature, K
u, v	velocity components, m/s
x, y	cartesian coordinates, m

Greek letters

α	thermal diffusivity, m²/s
β	thermal expansion coefficient, 1/K
γ	magnetic field angle, °
θ	dimensionless temperature
λ	heat source parameter
μ	dynamic viscosity, Pa·s
ν	kinematic viscosity, m²/s
ρ	density, kg/m³
φ	nanoparticle volume fraction
ψ	stream function, m²/s
σ	electrical conductivity, S/m

Subscripts

avg	average
c	cold
f	base fluid
h	hot

hnf	hybrid nanofluid
nf	nanofluid
s	solid nanoparticle
total	total

Abbreviations

CFD	computational fluid dynamics
FEM	finite element method
MHD	magnetohydrodynamic
NEPCM	nano-encapsulated phase change material
PCM	phase change material